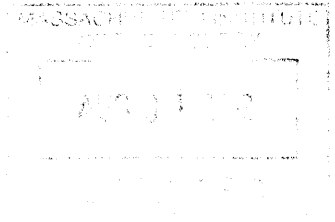


ARCHIVES



Contact-Printed Microelectromechanical Systems

by

Apoorva Murarka

B.Sc., Electrical Engineering, Massachusetts Institute of Technology (2010)

Submitted to the Department of Electrical Engineering and Computer Science

in partial fulfillment of the requirements for the degree of


Master of Engineering in Electrical Engineering and Computer Science


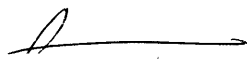
at the


MASSACHUSETTS INSTITUTE OF TECHNOLOGY

June 2012

© Massachusetts Institute of Technology 2012. All rights reserved.

Author 
Department of Electrical Engineering and Computer Science
May 25, 2012

Certified by  
Professor of Electrical Engineering and Computer Science
Thesis Supervisor

Accepted by 
Professor Dennis M. Freeman
Chairman, Masters of Engineering Thesis Committee

Contact-Printed Microelectromechanical Systems

by

Apoorva Murarka

Submitted to the Department of Electrical Engineering and Computer Science on

May 29, 2012

in partial fulfillment of the requirements for the degree of

Master of Engineering in Electrical Engineering and Computer Science

ABSTRACT

Microelectromechanical systems (MEMS) are ubiquitous. Scalable large-area arrays of MEMS on a variety of substrates, including flexible substrates, have many potential applications. Novel methods for additive fabrication of thin (125 ± 15 nm thick) suspended gold membranes on a variety of rigid and flexible cavity-patterned substrates for MEMS applications are reported. The deflection of these membranes, suspended over cavities in a dielectric layer atop a conducting electrode, can be used to produce sounds or monitor pressure. The reported fabrication methods employ contact-printing, and avoid fabrication of MEMS diaphragms via wet or deep reactive-ion etching, which in turn removes the need for etch-stops and wafer bonding. Elevated temperature processing is also avoided to enable MEMS fabrication on flexible polymeric substrates. Thin films up to 12.5 mm^2 in area are fabricated. The MEMS devices are electrically actuated and the resulting membrane deflection is characterized using optical interferometry. Preliminary sound production is demonstrated, and further applications of this technology are discussed.

Thesis Supervisor: Vladimir Bulović

Title: Professor of Electrical Engineering and Computer Science

Acknowledgments

First, I would like to thank my advisor, Professor Vladimir Bulović. His advice, support, patience, humor, and encouragement over the past four years have been invaluable. I would also like to thank him for providing me with the opportunity and the resources to carry out the research that I love so much. Additionally, I am grateful for his willingness to entertain some of the crazier ideas involving my research from time to time. I look forward to growing as a researcher under his mentorship during my forthcoming Ph.D. years.

Next, I would like to thank Professor Jeffrey Lang for all of the valuable time he has spent on countless technical discussions concerning my research and its potential applications. His enthusiasm for this project has constantly fueled its progress. A great deal of the analysis performed in this thesis is a direct result of his intense guidance and assistance. Additionally, I am greatly indebted to him for helping me with countless revisions of my papers, posters, and presentations. I look forward to further evolving my approach to engineering problems under his guidance during my Ph.D. years.

I would also like to thank current and former members of the Organic and Nanostructured Electronics Lab for making research and work so enjoyable. Special shout outs to Annie, Farnaz, Joel, Yasu, Tim, Trisha, Wendi, Geoffrey, Jill, Andrea, Costi, and Eletha. Patrick—thank you for being such a great friend and a colleague. Special thanks go out to Corinne Packard, Vanessa Wood, Matt Panzer, Alexi Arango, Scott Bradley, and Sarah Paydavosi for showing me the ropes in lab when I was a UROP.

Special thanks go out to Ms. Anne Hunter, Ms. Linda Sullivan, and Ms. Vera Sayzew for all of the help and advice given during my undergraduate and M.Eng. years at MIT, and for ensuring that I graduated on time!

Additionally, I would like to thank all of my friends, and in particular Amey, Chintan, Adam, and Sagar, for all of the support, the discussions, and the fun!

Special thanks also go out to Mr. Ravi Meattle—his confidence in my abilities is reassuring.

Finally, I would like to thank my father and my late mother for their support and advice. They have had a great impact in shaping me while giving me the freedom to develop my own interests.

Contents

1	Microelectromechanical Systems	23
1.1	Microcontact Printing of MEMS	25
1.2	Prior Work and State of the Art	26
2	Modeling of PDMS Spacer Layer Pressure Sensors	31
3	MEMS Fabrication on PDMS Spacer Layers	39
3.1	Photolithography Transparency Masks	39
3.2	SU-8 Master Molds	40
3.3	Pick-up Stamp Substrates	41
3.4	Transfer Pad with Raised Mesas	42
3.5	Contact Lift-Off Transfer	43
4	PDMS Spacer Layer Device Characterization	47
5	Contact-Transfer Printed MEMS Membranes on Silicon Dioxide	53
5.1	Prior Work and State of the Art	54
5.2	The Acetone-Assisted Contact-Transfer MEMS Fabrication Process	55
5.2.1	Device Design	56
5.2.2	Pick-up Stamp Substrates	57

5.2.3	Transfer Pad with Raised Mesas	58
5.2.4	Contact Lift-Off Transfer	59
6	Silicon Dioxide Spacer Layer Device Characterization	63
6.1	Analysis	68
6.1.1	Determining Young's Modulus	68
6.1.2	Potential Sound Pressure Level Output	70
7	Quality of Contact-Printed Films on Silicon-based Substrates	73
7.1	Surface Roughness of Transferred Gold Films	73
7.2	Defects in Gold Films Transferred onto Cavity-Patterned Substrates	77
7.2.1	Irreversible Stiction of Gold Films to Cavity Sidewalls and Cavity Bottom	77
7.2.2	Excessive Stretching of Gold Membranes over Cavities . .	82
8	A Prelude to Contact-Printed Acoustics	87
8.1	Sound Production	91
9	Avenues for Further Research	95
9.1	Device Geometry	95
9.2	Transfer of Films of Different Metals and Graphene	96
9.3	Stamping Apparatus	97
9.4	Fabrication on Substrates with Patterned ITO-Electrodes	97
9.5	Phased Arrays of Sound Sources and Beam Steering	98
9.6	Demonstration as Microphones	99
9.7	Manipulation of Light Incident on a Surface	100

List of Figures

1.1	An overview of the microcontact printing process. The stamp consists of a PDMS layer that has been patterned with ridges that are about 25 μm wide, with 25 μm spacings between the ridges. The transfer pad consists of a viscoelastic substrate, such as PDMS, coated with an organic release layer, upon which a thin film of metal has been evaporated. The stamp is brought into contact with the metal film on the transfer pad, and it is rapidly peeled away, picking up the metal film from the transfer pad. The metal film bridges the gaps across the ridges in the PDMS if the stamp is peeled away from the donor transfer pad fast enough. The diagram above is not drawn to scale.	26
1.2	Process flow for contact lift-off transfer, as demonstrated by Packard, Murarka, et al. The last picture in the process flow shows that the PDMS ridges on the stamp are bridged by the lifted-off gold membrane, with air gaps between the ridges and beneath the membrane. The resulting MEMS variable capacitor can be used as a component of a variety of sensors [1].	29

1.3	Capacitance-voltage measurements for two devices (inset: geometry) tested as MEMS variable capacitors. As the voltage across the device increases, the electrostatic force of attraction between the gold membrane and the ITO electrode increases, causing the gold membrane to bow. The bowing of the gold membrane decreases the spacing between the two electrodes of the capacitor, hence, increasing the capacitance. Image courtesy [1].	30
1.4	Images of the devices formed by the Contact-Transfer process. a,c) Optical microscopy images of completed devices that act as variable capacitors. b) A schematic of completed devices. d) Photograph of devices fabricated on a flexible substrate [1].	30
2.1	A cross-sectional schematic of the air cavity and the surrounding PDMS support structure, being bridged by a gold membrane. The diagram is not drawn to scale.	32
2.2	An electrical model of the air cavity and the surrounding PDMS support structure shown in Figure 2.1.	32
2.3	When pressure is applied perpendicular to the plane of the circular membrane, it deflects. The maximum deflection, w_{max} , occurs at the center of the circular membrane. This figure is not drawn to scale.	34
2.4	We can group many small air cavities together in a PDMS substrate and electrically connect them in parallel by covering them with a common gold film electrode. The gold film is a parallelogram in shape so that it can completely cover the maximum number of air cavities while minimizing the capacitance from the surrounding PDMS. The figure is not drawn to scale.	37

3.1	An optical microscopy image of a pick-up stamp before pick-up of gold membrane. Each circular air cavity in the PDMS layer is about 12.5 μm in radius, and there is a spacing of at least 5 μm between the perimeters of adjacent cavities.	42
3.2	An optical microscopy image showing a raised parallelogram PDMS mesa on a PDMS transfer pad, before TPD and gold are evaporated on it. The gold electrode picked-up from this mesa will cover about 256 circular air cavities, each of radius 12.5 μm . The same transfer pad also has bigger parallelogram mesas that have areas that are four times larger than the area of the mesa shown above.	43
3.3	The process flow for the contact lift-off mesa-transfer micro-contact printing process. The drawings above are not to scale.	45
3.4	Scanning electron micrographs of (a) the SU-8 master mold, (b) a corner of the transfer pad parallelogram mesa with an organic film and a gold film evaporated on top, (c) the cavity-patterned PDMS spacer layer of the pick-up stamp, and (d) the edge of a transferred gold film bridging the air gaps in the PDMS spacer layer of the pick-up stamp.	46
4.1	Optical microscopy images contrasting the edge definition of devices fabricated using the old shadow-masking process and the new mesa-transfer process. a) Gold electrode of the MEMS device fabricated using shadow-masking. The edges of the electrode have poor definition. b) Gold electrode of the MEMS device fabricated using mesa-transfer. The edges of the electrode are much sharper and have sub-micron edge roughness.	48

4.2	An optical microscopy image of the pressure sensor fabricated using the contact lift-off mesa-transfer process. The gold parallelogram is the pressure sensor. Sags are visible in the gold membrane above the circular cavities. About 1024 circular cavities are covered by this parallelogram gold membrane which is about 140 nm thick. The mesa-transfer process enables the printing of sharp corners, with sub-micron edge roughness. The underlying PDMS on ITO-Glass is patterned with 25 μm diameter circular cavities with about 5 μm to 7 μm spacing between the circles. The circular cavities are arranged in a hexagonal-close-packed pattern.	49
4.3	Three capacitance-voltage sweeps for a single device. The approximate two-fold increase in the capacitance of the device with voltage indirectly demonstrates deflection of the gold membrane, which bows under the electrostatic force to decrease the gap spacing over the air cavities in the PDMS spacer layer, thus increasing the capacitance.	50
4.4	Optical microscopy images of gold membrane deflection under electrical actuation, as the voltage applied is increased. The membrane is being imaged from the back of the device, through the transparent, ITO-coated glass substrate. The membrane pulls in at voltages greater than 90 V. .	51
5.1	The process flow for the acetone-assisted, contact-transfer MEMS printing process on silicon-based substrates. The drawings above are not to scale.	60
5.2	A contact profilometry scan of the pick-up stamp. The pick-up stamp consists of a 400 nm thick silicon dioxide spacer layer on a silicon substrate. The silicon dioxide spacer layer is patterned with circular cavities in a hexagonal-close-packed arrangement.	61

6.1	Optical microscopy image of a $\sim 0.8\text{mm}^2$ area gold membrane MEMS device printed on silicon dioxide using the acetone-assisted contact-transfer process.	64
6.2	Deflection profiles of gold membranes under electrostatic actuation, obtained via optical interferometry. The height values shown above are offset by about 60 nm due to the presence of transparent oxide in the cavity reference region used by the interferometer. The deflection values, however, are absolute, i.e., about 60 nm should be subtracted from each point on each deflection curve above. (a) Deflection of the membrane increases as the voltage applied between the membrane and the Si substrate increases. (b) 13 different diametrical deflection profiles (inset: interferometry image) of a membrane under 15 V actuation, are plotted and averaged to show the mean profile. (c) Gold membrane deflection over multiple cavities covered by a single membrane, as the voltage is increased from 1 V to 15 V.	66
6.3	Optical interferometry images of several cavities under 15 V peak-to-peak amplitude sinusoidal voltage actuation at 15 Hz, taken at 30° phase intervals. Membrane deflection for only one half of a sine wave is shown in this figure. Each cavity is about $27\ \mu\text{m}$ in diameter.	67
6.4	A 3-D image of a gold film deflected over circular cavities, obtained using optical interferometry. The maximum deflection of the gold film is about 150 nm in the center, under 15 V bias. The diameter of each circular cavity is about $27\ \mu\text{m}$	68
6.5	Equation 6.1 fitted to the profile of a deflected membrane at 15 V bias, obtained via optical interferometry.	69

- 7.1 An optical interferometry image of a $630\ \mu\text{m} \times 473\ \mu\text{m}$ region of a gold film transferred onto a planar silicon substrate, without any tilt correction. This region of the transferred film has an average surface roughness of 9.24 nm and a root mean square roughness of 11.45 nm. 75
- 7.2 An optical interferometry image of a $630\ \mu\text{m} \times 473\ \mu\text{m}$ region of a gold film (as shown in Figure 7.1), with tilt correction applied. The average surface roughness of the same region decreases to 1.94 nm, and the root mean square roughness decreases to 3.03 nm when tilt correction is applied. 76
- 7.3 Optical interferometry images of the same transferred gold film taken at different magnifications. (a) A $1.2\ \text{mm} \times 0.87\ \text{mm}$ region of a transferred gold film with an average surface roughness of 2.27 nm and a root mean square roughness of 3.61 nm. (b) A $319\ \mu\text{m} \times 239\ \mu\text{m}$ region of the same film with an average surface roughness of 1.81 nm and a root mean square roughness of 3.03 nm. (c) A $630\ \mu\text{m} \times 473\ \mu\text{m}$ region of the same transferred gold film with an average surface roughness of 1.94 nm and a root mean square roughness of 3.03 nm, as shown in Figure 7.2 also. (d) A $50\ \mu\text{m} \times 48\ \mu\text{m}$ subregion of the film in (c) that is largely free from processing residue or specks. The average surface roughness of this subregion is reduced to 1.32 nm and the root mean square roughness is reduced to 1.60 nm. 78

7.4 An optical interferometry image of a gold film contact-printed onto a cavity-patterned silicon dioxide spacer layer. Two main types of defects are observed. The gold film collapses over some cavities as it sticks to the cavity sidewalls and to the cavity bottom. This collapse of the gold film causes it to stretch irreversibly. The uncollapsed gold film over a cavity is excessively stretched when that cavity is surrounded by other cavities over which the gold film has collapsed. The excessive stretching causes the gold film to take on a peculiar shape, best described as a ‘ridge’ surrounded by a ‘basin’ on either side. The direction of the ridge is determined by the direction of excessive tension. Therefore, the ridge usually runs between two cavities with collapsed gold films, as shown above. If a cavity is surrounded by more than two cavities with collapsed membranes, then the direction of the ridge over the ‘sandwiched’ cavity is offset to account for the excessive tension from the surrounding collapsed-membrane cavities. 79

7.5 An optical interferometry image of a gold film that has collapsed over one of the cavities during the fabrication process. The thin green ring near the perimeter of the cavity indicates that the sunk-in gold film is nearly vertical at the cavity perimeter, as corroborated by the cross-section profile in Figure 7.6. 80

7.6 Cross-section profiles of a gold membrane that has collapsed over a cavity during the fabrication process. The vertical distance from the gold membrane on top of a silicon dioxide support (in between adjacent cavities) to the gold membrane at the bottom of a cavity is about 950 nm, as indicated above. This implies that the gold membrane sinks all the way to the bottom of the cavity. 81

7.7 Optical interferometry images of an over-stretched gold film over a ‘sandwiched’ cavity, as shown in Figure 7.4. The cavity shown is surrounded by two cavities (not shown) over which the gold film has collapsed during the fabrication process. (a) A 2-D image of the sandwiched cavity. (b) A 3-D image of the sandwiched cavity obtained using interferometry data to highlight the elevated regions (the ridge) and the depressed regions (the basins) of the over-stretched gold film. The ridge spans the diameter of the cavity, and the two surrounding cavities over which the gold film has collapsed, are at either end of the ridge, as indicated by the points A and A’ on the figure. 83

7.8 Cross-section profiles of the over-stretched gold membrane across a sandwiched cavity, as discussed in Figure 7.7. The profile in red is across the basins and the ridge of the gold membrane, showing that the ridge rises about 200 nm above the planar surface of the gold film and that the deepest point in the basins is about 300 nm below the planar surface of the gold film resting on the silicon dioxide supports. The profile in blue is across the length of the ridge. 84

7.9	(a) Optical interferometry image of a gold membrane deflected over 400 nm deep cavities under 15 V applied bias. The white line indicates the cavities for which the deflection is plotted in (b) over various applied voltages. This line of cavities (A-E) is next to a cavity over which the gold membrane has collapsed due to fabrication, as indicated by 'X'. (b) Gold membrane deflection over multiple cavities as the voltage applied is increased from 1 V to 15 V. The deflection of the gold membrane over a cavity (E) next to a collapsed-membrane cavity (X) is significantly smaller than that of the membrane over cavities (A-D) further away from the collapsed-membrane cavity.	85
8.1	Photographs of large area gold membrane devices fabricated on cavity-patterned silicon dioxide substrates via acetone-assisted contact-transfer printing with increased transfer pad curing time and spacer layer silanization time, increased silane concentration, and increased silanization temperature. (a) A large area gold membrane covering about 16000, 27- μ m-diameter cavities, in a single-sensor geometry. (b) and (c) Arrays of large area gold membranes, each covering about 4000, 27- μ m-diameter cavities.	90
8.2	Photographs of two approximately 0.5" \times 0.5" silicon substrates that are extensively covered in gold films transferred via the modified acetone-assisted contact-transfer process. The yield (the area of gold picked-up and transferred per substrate) increases significantly due to the modification of transfer pad fabrication and spacer layer silanization parameters.	90

8.3	The electrical setup for preliminary sound production tests. The signal is being applied to the contact-printed device from the waveform generator via a high voltage amplifier. Electrical contact to the device is made using soft gold wire probes. Silver paste is used to improve electrical contact between the device substrate and the grounded aluminum foil.	91
8.4	The far-field beampattern for an unphased, two-dimensional, rectangular array of sound producing elements obtained by computing the 2-D discrete Fourier transform (DFT) of the rectangular array. The narrow main lobe in the beampattern suggests that the loudest sound is heard on-axis, that is, directly above the gold film of the contact-printed device.	92
8.5	A cross-section schematic of a MEMS device with a contact-printed metal film. The thickness of the film varies across the length of the film such that multiple cavities or gaps are bridged by a single film of varying thickness. The bridged cavities can be commonly actuated or each cavity can be addressed individually. The drawing above is not to scale.	94
9.1	An illustration of a large-area array of individually-addressable sensors (or actuators) fabricated on a flexible substrate. Each element in the array can be addressed via the row-selecting and column-selecting multiplexers.	98
9.2	A simple current-sensing circuit implemented using an op-amp differentiator to detect capacitance changes of the MEMS device in response to an incident sound pressure wave.	99

9.3	When the deflection, h , of the metal membrane is large enough, a significant portion of the reflected light intensity decreases due to interference, thus making the membrane covered surface appear rough. The devices discussed in Chapter 6 are able to achieve deflections that are large enough to produce the aforementioned effect for a wide spectrum of visible light, for angles of incidence up to 60°	101
9.4	The blue arrows represent incident light and the black arrows represent reflected light. The metal membrane can be made to deflect asymmetrically by switching ON only one of the two electrodes, A or B. The asymmetrical deflection causes the normal of the reflecting surface to rotate, hence, changing the direction in which the incident light is reflected. The degree of asymmetrical deflection can be increased or decreased by increasing or decreasing the voltage applied to the ON electrode. When both electrodes are switched on or switched off, most of the incident light is reflected back in the incident direction.	103

List of Tables

9.1	The minimum uniform deflection of metal membranes needed to make a reflecting surface appear rough through diffused reflection, for red, green, and blue light, at different angles of incidence of light.	102
-----	--	-----

Chapter 1

Microelectromechanical Systems

Microelectromechanical systems (MEMS) are devices that have components on the order of 1 micrometer to 100 micrometers in size that are typically fabricated on a silicon substrate. MEMS encompass a wide range of electronic sensors and actuators such as accelerometers, gyroscopes, pressure sensors, chemical sensors, etc. These devices are ubiquitous in consumer electronics such as hand-held gaming devices, gaming controllers, cellular phones, and camera-lens stabilizers. Accelerometers and gyroscopes are also used for vehicular stability and control in cars. MEMS also have a variety of industrial applications for precise measurement of linear and rotational motion and detection of forces, air and gas pressures, and other physical phenomenon. It is desirable to extend the functionality of MEMS to different form factors including large area arrays of sensors and actuators, and various substrate materials. Large area MEMS consist of arrays of numerous MEMS devices fabricated on a single substrate. Each MEMS device in an array acts as an individual sensor and senses the physical phenomenon such as force or pressure in its immediate local area. Therefore, all the sensors in a large area array can provide information about the physical phenomenon as it varies across

the large area of the array. However, scalable large area MEMS have yet to be fabricated cost-efficiently, and on substrates other than silicon. Large area MEMS arrays have a variety of potential applications—they can be used as phased-array sensors for acoustic imaging, as sensor skins in humans and vehicles, and for wind-tunnel testing [1]. Conventionally, pressure sensors are placed at a finite number of points on a surface of a body that is being tested in a wind-tunnel. The data from these finite number of pressure sensors is then extrapolated to deduce the air pressure conditions at areas between the pressure sensors. Large area MEMS arrays reduce the need for the extrapolation of sensor data due to the high spatial resolution of the sensors in these arrays, thus enabling pressure to be sensed across the surface of the body with greater accuracy. Additionally, in order to fabricate large-area sensor arrays that can act as sensor skins and conform to the shape of the vehicle or the human body, it is desirable to fabricate these arrays on a flexible substrate, such as polymeric substrates [1].

Even though MEMS on scalable, large area substrates or on flexible substrates are desirable and have a great variety of potential applications, standard MEMS fabrication processes are incompatible with plastic substrates. Conventional fabrication of MEMS devices involves processes that are typically used in microelectronics fabrication [1], and are centered around using silicon as the substrate upon which these devices are fabricated [2]. Processing of silicon to fabricate MEMS devices often involves photolithography, harsh chemical etches, and elevated temperature processing [1] for the growth of oxides and the deposition of polysilicon. Additionally, since conventional microelectronics fabrication is limited to conventional silicon wafer sizes [3], it is difficult to scale the area of arrays of MEMS sensors to any particular size. Moreover, the harsh chemical etches and the elevated temperature processing make it difficult to fabricate MEMS devices on

flexible substrates that degrade under such processing.

Fabrication of flexible electronics using silicon processing techniques involves fabricating the electronics on a silicon substrate and then bonding these structures to flexible sheets. These structures are then released from the silicon substrate by breaking small supports or by etching away a sacrificial layer [4]. However, this process has not been used for MEMS fabrication.

1.1 Microcontact Printing of MEMS

Printing techniques which involve flexible polymeric stamps, like the ones employed by Rogers [4][5], fall under the more general category of microcontact printing or soft lithography. Such techniques show promise for the patterning or transfer of microscale films of a variety of materials. Microcontact printing can be utilized for the fabrication of large area MEMS arrays on a variety of substrates, including silicon. The approach to microcontact printing presented here involves the use of a stamp and a donor transfer pad. The donor transfer pad consists of a viscoelastic material coated with an organic release layer. A thin film of metal is then deposited on top of the organic release layer via evaporation. The stamp consists of a layer of patterned PDMS atop a glass slide that is coated with a layer of electrically conducting indium tin oxide (ITO). The surface of this patterned PDMS stamp is placed in contact with the thin metal film on the donor transfer pad and then the stamp is rapidly peeled away, picking up the metal film. The metal film ends up bridging the gaps in the patterns of the PDMS stamp, forming a capacitive MEMS structure. A continuous film of metal is lifted off onto the stamp only if the stamp is peeled off from the transfer pad rapidly, as discussed in References [4][5], where it is shown that a rapid peel rate greater than 5 ms^{-1} en-

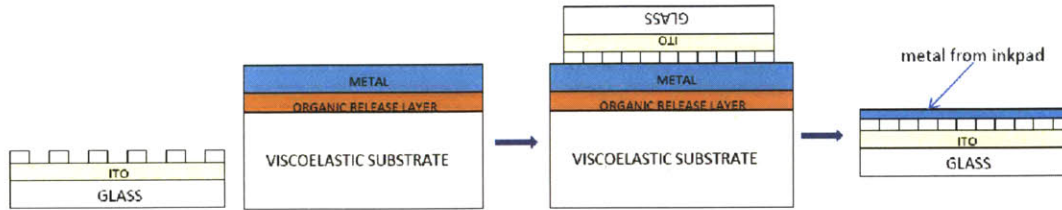


Figure 1.1: An overview of the microcontact printing process. The stamp consists of a PDMS layer that has been patterned with ridges that are about $25\ \mu\text{m}$ wide, with $25\ \mu\text{m}$ spacings between the ridges. The transfer pad consists of a viscoelastic substrate, such as PDMS, coated with an organic release layer, upon which a thin film of metal has been evaporated. The stamp is brought into contact with the metal film on the transfer pad, and it is rapidly peeled away, picking up the metal film from the transfer pad. The metal film bridges the gaps across the ridges in the PDMS if the stamp is peeled away from the donor transfer pad fast enough. The diagram above is not drawn to scale.

hances adhesion between a viscoelastic polymer and silicon thin film components and allows these thin film components to be lifted off from the substrate and onto the viscoelastic polymer.

Microcontact printing does away with the harsh chemical etches and the elevated temperature processing typical of conventional MEMS fabrication techniques. In fact, most of the processing after the organic and metal deposition can be carried out at room temperature and pressure conditions. This enables the use of a variety of substrates that would otherwise degrade at high temperatures and pressures, such as flexible polymeric substrates. Additionally, since we are no longer restricted to silicon substrates, the size of the substrates can be scaled easily, enabling the fabrication of large-area sensor arrays.

1.2 Prior Work and State of the Art

In the Bulovic research group, we demonstrate the fabrication of a MEMS capacitor structure using the contact lift-off transfer (Contact-Transfer) technique. The

Contact-Transfer technique relies on the rapid removal of the patterned PDMS stamp from the donor transfer pad to effect the transfer of a continuous film of gold from the donor transfer pad to the patterned PDMS stamp. The rapid removal of the patterned PDMS stamp is essential for the transfer of a continuous gold film because the adhesion between the gold film (on the transfer pad) and the PDMS ridges on the stamp is enhanced by a rapid peel rate. The removal of the gold thin film from the transfer pad is also enhanced due to the weak van der Waals bonding between the gold film and the organic release layer underneath it on the transfer pad. This weak van der Waals bonding between the gold film and the organic release layer is overcome by the kinetically controlled adhesive forces between the PDMS ridges and the gold film, allowing the transfer of a continuous film of gold that bridges the gaps between the PDMS ridges on the stamp. This continuous gold film atop the air gaps between the PDMS ridges is flexible and it can deflect in response to pressure. The resulting structure is a variable capacitor that can be used as a MEMS device for sensing acceleration, pressure, sound waves, and other physical phenomenon.

The organic used for the release layer is N,N'-diphenyl-N,N'-bis(3-methylphenyl)-(1,1'-biphenyl)-4,4'-diamine (TPD). The TPD organic release layer is 90 nm thick and the gold film is ~140 nm thick. The above technique is demonstrated for three different sets of stamps. The first set of stamps has PDMS ridges that are 45 μm wide, 25 μm apart and 1.2 μm high, with an underlying layer of PDMS that is 1.8 μm thick. The second set of devices has PDMS ridges that are 20 μm wide, 20 μm apart and 2.2 μm high, with an underlying layer of PDMS that is 12 μm thick. Both of these stamps are fabricated on an ITO-coated glass substrate. The third set of stamps is fabricated on a flexible, ITO-coated, 175- μm -thick polyethylene terephthalate substrate [1]. Refer to Figure 1.2 for fabrication details. The oxygen

plasma exposure time for the flexible substrate is reduced to 1 minute. All other fabrication steps for the flexible substrate devices are the same as those for the glass substrate devices.

Using the above-mentioned process flow, we fabricate a variable capacitor structure whose capacitance varies from about 4.4 pF to 4.8 pF as the voltage is swept from 0 V to 100 V, as shown in Figure 1.3. The resulting devices are shown in Figure 1.4.

The fabricated MEMS variable capacitor can be used to sense air and gas pressures. Thus, the next step is to model these capacitors as pressure sensors that are capable of producing a measurable change in capacitance in response to a range of applied pressures. Once the MEMS capacitors are modeled as pressure sensors, a fabrication process is designed for fabricating these devices using microcontact printing. Additionally, the fabrication steps are improved to remove the edge effects that are present at the edges of the lifted-off gold membranes, as seen in Figure 1.4. The poor edge-definition compromises control of the device geometry. The edge-definition is poor because the gold membrane decreases in thickness at its edges due to the deposition of the gold on the donor transfer pad via a shadow mask. The current process, termed mesa-transfer, reduces the edge roughness of the lifted-off gold membrane, and is used to fabricate capacitive MEMS structures. These micro-contact printed structures are then characterized as pressure sensors by demonstrating the deflection of the printed gold membranes via electrostatic actuation.

Contact-Transfer

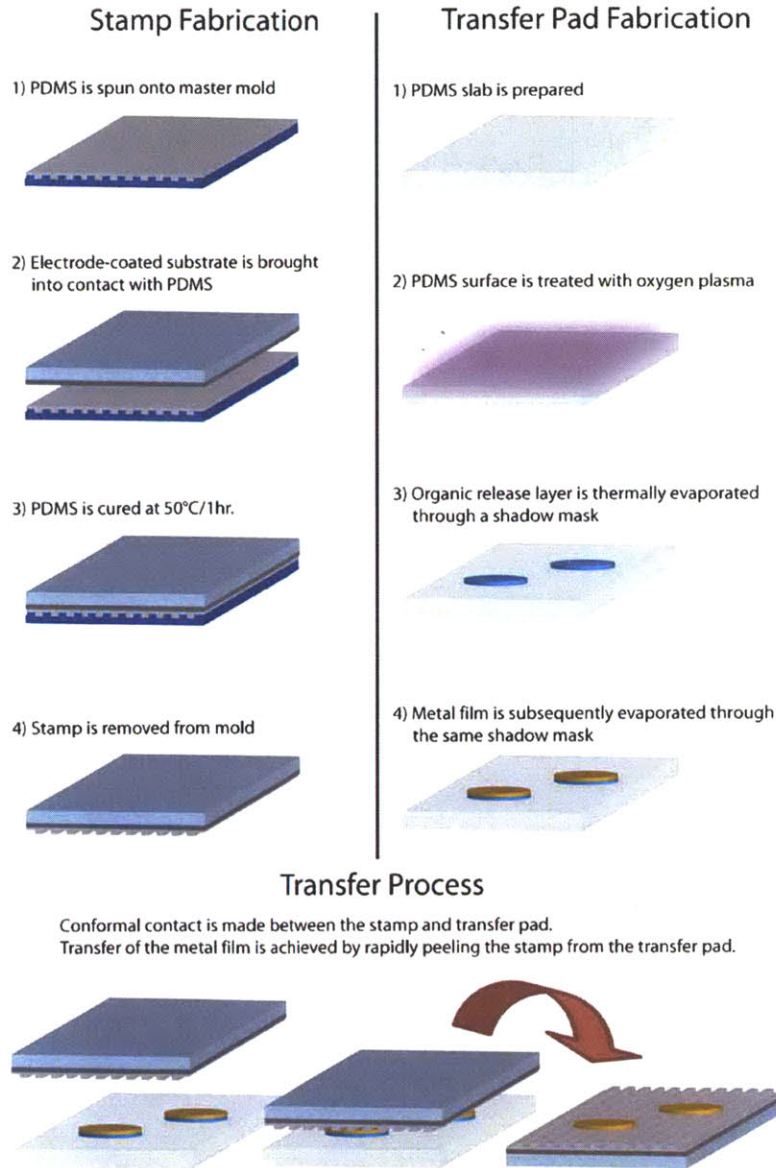


Figure 1.2: Process flow for contact lift-off transfer, as demonstrated by Packard, Murarka, et al. The last picture in the process flow shows that the PDMS ridges on the stamp are bridged by the lifted-off gold membrane, with air gaps between the ridges and beneath the membrane. The resulting MEMS variable capacitor can be used as a component of a variety of sensors [1].

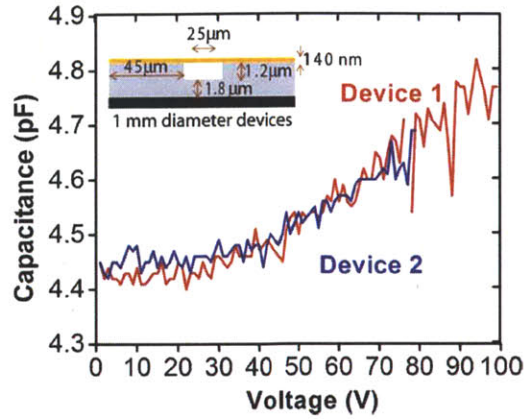


Figure 1.3: Capacitance-voltage measurements for two devices (inset: geometry) tested as MEMS variable capacitors. As the voltage across the device increases, the electrostatic force of attraction between the gold membrane and the ITO electrode increases, causing the gold membrane to bow. The bowing of the gold membrane decreases the spacing between the two electrodes of the capacitor, hence, increasing the capacitance. Image courtesy [1].

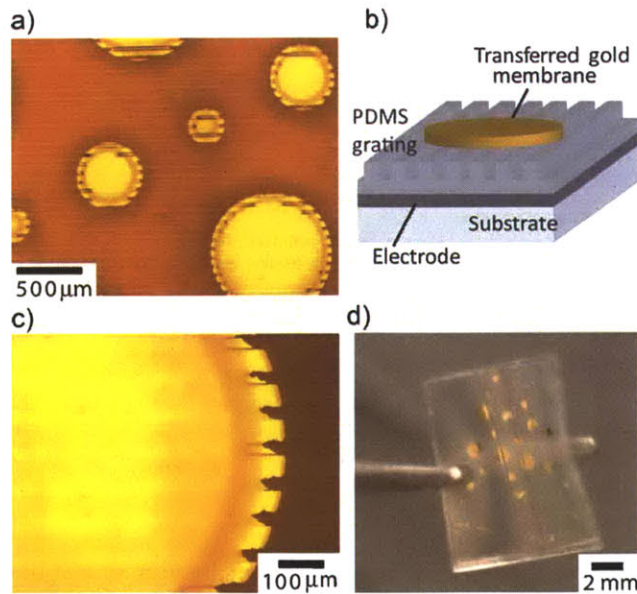


Figure 1.4: Images of the devices formed by the Contact-Transfer process. a,c) Optical microscopy images of completed devices that act as variable capacitors. b) A schematic of completed devices. d) Photograph of devices fabricated on a flexible substrate [1].

Chapter 2

Modeling of PDMS Spacer Layer

Pressure Sensors

The variable capacitor MEMS structure fabricated via microcontact printing can be used to sense pressure as the gold membrane of the structure deflects in response to applied pressure, hence changing the capacitance of the device. These MEMS variable capacitors are modeled as pressure sensors that are capable of producing a measurable change in capacitance for a range of applied pressures. This implies that the membrane of the variable capacitor should be able to bow enough to produce a measurable change in capacitance under pressures between 2 psi to 30 psi, without breaking, or losing its elasticity. The pressure range is chosen to reflect the conditions most commonly encountered in wind-tunnel testing, with the aim that these devices might eventually be suitable for fabricating sensor skins for vehicular wind-tunnel testing.

The pressure sensor MEMS device is modeled as a circular cavity in a PDMS spacer layer that sits atop an ITO-coated glass substrate. This cavity is bridged by a gold membrane that serves as the top electrode that deflects in response

to air pressure, as shown in Figure 2.1. The circular air cavity and its PDMS supports are electrically modeled as two capacitors, C_1 and C_2 , in parallel with each other, as shown in Figure 2.2. Capacitor C_1 comprises the capacitance of the PDMS support structures that surround the air cavity in the PDMS layer. This capacitance is assumed constant and it does not change in response to applied pressure. Capacitor C_2 consists of the capacitance of the air gap, C_{air} , in series with the capacitance of the underlying residual PDMS layer, C_{PDMS} . This residual PDMS layer tends to act as a dielectric layer in capacitor C_2 . The capacitance C_{air} changes in response to applied air pressure.

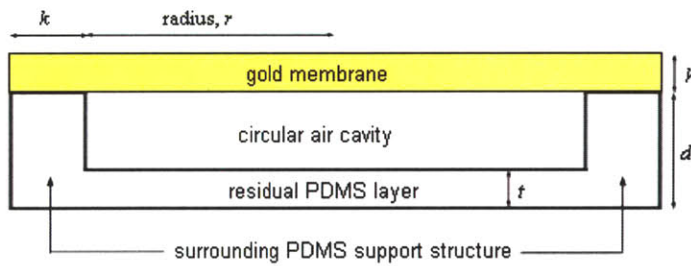


Figure 2.1: A cross-sectional schematic of the air cavity and the surrounding PDMS support structure, being bridged by a gold membrane. The diagram is not drawn to scale.

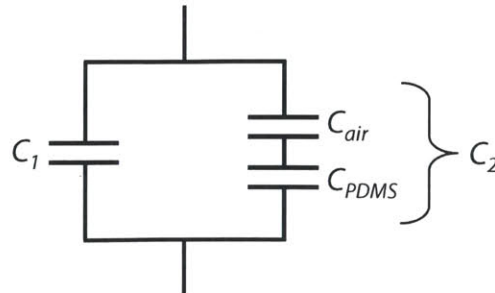


Figure 2.2: An electrical model of the air cavity and the surrounding PDMS support structure shown in Figure 2.1.

The capacitance of C_1 is given by,

$$C_1 = \frac{\varepsilon_0 \varepsilon_{PDMS} A_{support}}{d} = \frac{8.854 \times 10^{-12} \cdot 2.55 \cdot A_{support}}{d}, \quad (2.1)$$

where $\varepsilon_0 = 8.854 \times 10^{-12}$ (permittivity of free space), $\varepsilon_{PDMS} = 2.55$ (dielectric constant of PDMS [6]), $A_{support}$ is the area of the PDMS supports surrounding the circular cavity, and d is the distance between the top and bottom electrodes as defined in Figure 2.1.

The capacitance of C_2 is given by,

$$C_2 = \frac{\varepsilon_0 \varepsilon_{PDMS} A_{membrane}}{\varepsilon_{PDMS} (d - t) + t}, \quad (2.2)$$

where d is the distance between the top and bottom electrodes, t is the thickness of the residual PDMS layer in the air cavity as defined in Figure 2.1, and $A_{membrane}$ is the area of the circular gold membrane that can deflect.

Since capacitances in parallel add, the net capacitance, C_{device} , of the air cavity and its surrounding PDMS is given by,

$$C_{device} = C_1 + C_2 = \frac{\varepsilon_0 \varepsilon_{PDMS} A_{support}}{d} + \frac{\varepsilon_0 \varepsilon_{PDMS} A_{membrane}}{\varepsilon_{PDMS} (d - t) + t}. \quad (2.3)$$

If the circular cavity has a diameter of 1 mm and a surrounding annular PDMS support structure of width $k = 0.1$ mm, then substituting $d = 5 \mu\text{m}$ and $t = 3 \mu\text{m}$ into Equation 2.3 yields a device capacitance, C_{device} , of about 3.7 pF. A 0.1 pF change in the capacitance of the above-modeled air cavity is desired when pressure is applied because a change of 0.1 pF can be measured easily by test circuitry. Assuming uniform deflection of the gold membrane across its entire area—that is, the gold membrane deflects by equal amounts everywhere across its surface—then

a deflection of about 140 nm is needed to observe a change of 0.1 pF. However, in reality, when pressure is applied on a circular membrane, it deflects the most at its center and the least towards its edges. Hence, in reality for a 140 nm deflection of the gold membrane at its center, a change in capacitance of less than 0.1 pF for the whole device is expected.

The deflection of a circular membrane (that is supported at its edges) of radius r , when a uniformly distributed force is applied perpendicular to the plane of the membrane is shown in Figure 2.3 [7]. The membrane is assumed to be under tension before the force is applied. Additionally, it is also assumed that the deflection is purely elastic and recoverable, with no permanent deformation.

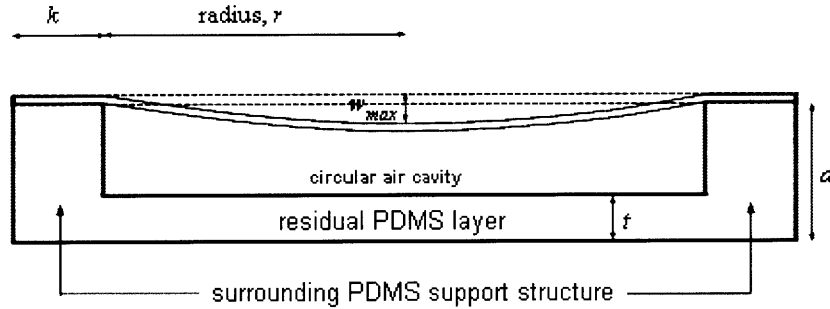


Figure 2.3: When pressure is applied perpendicular to the plane of the circular membrane, it deflects. The maximum deflection, w_{max} , occurs at the center of the circular membrane. This figure is not drawn to scale.

The maximum deflection, w_{max} , at the center of a circular membrane of radius r , is given by,

$$w_{max} = \frac{(5 + \nu) q r^4}{64(1 + \nu) D}, \quad (2.4)$$

where q is the pressure distributed uniformly over the circular membrane surface, D is the flexural rigidity of the membrane, and ν is the Poisson's ratio for gold ($\nu = 0.42$).

The flexural rigidity of the membrane, D , in Equation 2.4 is given by,

$$D = \frac{E h^3}{12(1 - \nu^2)}, \quad (2.5)$$

where E is the modulus of elasticity of gold ($E = 78$ GPa), h is the thickness of the gold membrane, and ν is the Poisson's ratio for gold.

For an applied pressure of 10 psi, using the device geometries stated above for a 3.7 pF air cavity with surrounding PDMS supports, substituting $q = 10$ psi, $r = 0.5$ mm and $h = 140$ nm into Equations 2.4 and 2.5, yields a maximum deflection of 11.8 meters—a displacement that is significantly in excess of the air gap height and is, therefore, an unphysical result. Instead, a maximum deflection of about 150 nm is desired to reduce the likelihood of membrane rupture. Therefore, in order to decrease the maximum deflection of the gold membrane, the radius of membrane needs to be reduced by two orders of magnitude, the pressure applied needs to be reduced, and the flexural rigidity of the gold membrane needs to be increased by increasing the thickness of the gold membrane to about 200 nm. Thus, if $h = 200$ nm and the applied pressure, q , varies between 2 psi to 10 psi, the radius of the gold membrane needs to be between 7 μm and 10 μm for a maximum membrane deflection of 150 nm under the applied pressure. However, reducing the radius of the gold membrane from 0.5 mm to 10 μm greatly reduces the area of the variable capacitor that consists of the air cavity. The capacitance, C_{device} , of the air cavity and the surrounding annular PDMS supports is reduced by about three orders of magnitude to 2.1 fF as the radius of the cavity is reduced from 0.5 mm to 12.5 μm . This means that when the membrane deflects by 150 nm, only $\sim 6.8 \times 10^{-17}$ F of capacitance change results. We require around 0.1 pF of capacitance change for the same amount of deflection when 2 psi to 10 psi of pressure is applied.

Since capacitances add up in parallel, the changes in capacitances also add up. Thus, a multitude of these smaller air cavities can be arranged in parallel with each other to achieve the desired change in capacitance for ~ 150 nm of deflection under applied pressure. The air cavities can be electrically connected in parallel by covering them with a common gold film electrode. About 1500 of the above-modeled air cavities are needed in parallel with each other to form a single pressure sensor that is capable of providing a net 0.1 pF of capacitance change in response to a 150 nm membrane deflection in each of these 1500 cavities when 2 psi to 10 psi of pressure is applied.

It is necessary to pack all of these air cavities in as small a space as possible in the PDMS spacer layer atop the ITO-glass, in order to minimize the non-active capacitance due to the PDMS supports surrounding these air cavities. An efficient way to pack circular air cavities in a two dimensional plane is to use hexagonal close packing with a certain amount of fixed spacing between the perimeters of each of the air cavities, as shown in Figure 2.4. The gold film covering the air cavities has a parallelogram shape so that it can completely cover the maximum number of cavities while minimizing the capacitance from the surrounding PDMS spacer layer.

A 32×32 array of hexagonal-close-packed 1024 air cavities (each with a radius of $12.5 \mu\text{m}$) with a spacing, s , of $5 \mu\text{m}$ between the cavities, will have a total capacitance of 2.7 pF. A MEMS device comprising 1024 cavities will give a total of approximately 0.07 pF capacitance change when the gold membrane deflects uniformly by 150 nm. This 32×32 array will have a total area of 0.79 mm^2 , including the PDMS supports in between the air cavities. A 16×16 array of 256 hexagonal-close-packed air cavities will a total area that is a quarter the area of a 32×32 array. As a result, the capacitance of a 16×16 array with the same

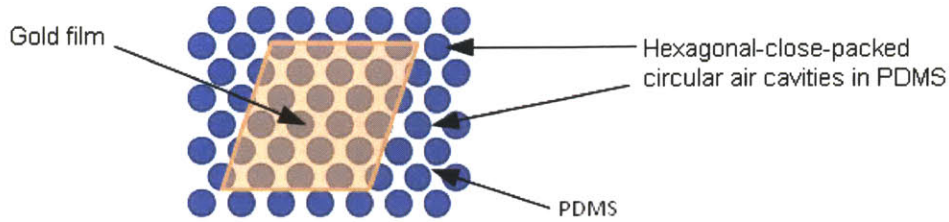


Figure 2.4: We can group many small air cavities together in a PDMS substrate and electrically connect them in parallel by covering them with a common gold film electrode. The gold film is a parallelogram in shape so that it can completely cover the maximum number of air cavities while minimizing the capacitance from the surrounding PDMS. The figure is not drawn to scale.

cavity radius and inter-cavity spacing (as a 32×32 array) will have a capacitance that is a quarter of the capacitance of a 32×32 array. A 16×16 array will give a total of approximately 0.0175 pF of capacitance change when the gold membrane deflects by 150 nm. For the initial device fabrication run, a $12.5 \mu\text{m}$ cavity radius (r), and a $5 \mu\text{m}$ inter-cavity spacing (s) is selected. These devices are used as a proof of concept and their characterization will enable more accurate modeling and fabrication of subsequent devices.

Chapter 3

MEMS Fabrication on PDMS

Spacer Layers

3.1 Photolithography Transparency Masks

The first step in the device fabrication process involves making the transparency masks that define the device (pressure sensor) geometries. These masks are used in ultraviolet (UV) photolithography for patterning photoresists. UV photolithography is used for making SU-8 masters, which are in turn used as molds for patterning the PDMS transfer pad and the PDMS spacer layer on the ITO-glass pick-up stamp. SU-8 is a negative photoresist. The portion of SU-8 resist that is exposed to light becomes insoluble to the SU-8 photoresist developer, propylene glycol monomethyl ether acetate (PGMEA). The unexposed portion of the SU-8 resist is dissolved away by the SU-8 developer. Two different transparency masks are made.

Mask A is designed to mold raised parallelogram mesas on the PDMS transfer pad. Thus, Mask A has dark parallelogram regions of varying areas. These dark

parallelogram regions on the mask result in parallelogram troughs in the SU-8 master, that in turn form raised parallelogram mesas on the PDMS transfer pad. Mask A has dark rhombuses of two different areas— 0.79 mm^2 and 0.1975 mm^2 . The internal angles of these rhombuses measure 60° and 120° to maximize the number of hexagonal-close-packed air cavities completely covered by each rhombus. Mask A is printed at a resolution of 5080 dpi by PageWorks (Cambridge, MA).

Mask B is designed to form circular air cavities in the PDMS spacer layer that is spun onto the ITO-glass stamp. Thus, cylindrical pillars need to be formed in the corresponding SU-8 master. Therefore, Mask B has transparent circular regions in a dark background. The transparent circles of $12.5 \text{ }\mu\text{m}$ radius are hexagonal-close-packed with a minimum spacing of $5 \text{ }\mu\text{m}$ between adjacent circles. Mask B is printed at a 65024 dpi resolution by FineLine Imaging (Colorado Springs, CO).

3.2 SU-8 Master Molds

SU-8 photoresist (MicroChem Corp., SU-8 3010) is spun onto two different silicon wafers separately to fabricate the SU-8 master molds for the pick-up stamp and the transfer pad. SU-8 photoresist is poured onto each silicon wafer and the wafer is spun at 1000 rpm such that the SU-8 covers the entire surface of the wafer. These wafers with the SU-8 layers are then spun at 3000 rpm for another 30 seconds, after which they are soft-baked on a hot plate at $95 \text{ }^\circ\text{C}$ for 5 minutes. Next, the wafers are allowed to cool for 2 minutes before being placed in an Amergraph UV exposure unit with either Mask A or Mask B placed on top of the SU-8 photoresist layer, with the mask emulsion in contact with the SU-8 layer. Mask A is used to make the SU-8 masters for the transfer pad and Mask B is used to make the

SU-8 masters for the pick-up stamp. The SU-8 photoresist is then exposed to UV light. After UV exposure, the wafers are baked on a hot plate for 2 minutes. The wafers are then immersed in SU-8 developer solution (PGMEA) for 4 minutes and agitated. After that, the wafers are sprayed with PGMEA for 10 seconds to rinse off residual SU-8, and with isopropanol for another 10 seconds to remove PGMEA. The wafers are dried with nitrogen and hard-baked for 3 hours at 150 °C on a hot plate to get the resulting SU-8 masters. Following the hard bake, both SU-8 master molds are silanized with trichloro(1H,1H,2H,2H-perfluorooctyl)silane (Sigma-Aldrich) to ensure easy removal of the cured PDMS [1].

3.3 Pick-up Stamp Substrates

Next, an indium tin oxide (ITO) coated glass slide is cleaned using the standard substrate cleaning procedure: sonication in Micro-90 for 5 minutes, followed by sonication in deionized water twice for 5 minutes each, followed by sonication in acetone twice for 2 minutes each, and followed by immersion in boiling isopropanol twice, for two minutes each. The ITO-glass slide is then blown dry with nitrogen and treated with oxygen plasma for 5 minutes. The pick-up stamp is fabricated by spinning uncured PDMS (Sylgard 184, Dow Corning Co.), mixed in a 10:1 base-to-curing-agent ratio by weight and degassed under vacuum, onto the silanized SU-8 master with cylindrical pillars (made using Mask B). The conducting side of the ITO-coated glass slide is then pressed firmly onto the spun PDMS atop the SU-8 master. The resulting structure is then placed in an oven at 60 °C for 4 hours to cure the PDMS between the SU-8 master and the ITO-glass. The pick-up stamp with circular air cavities in the cured PDMS layer is then removed from the SU-8 master.

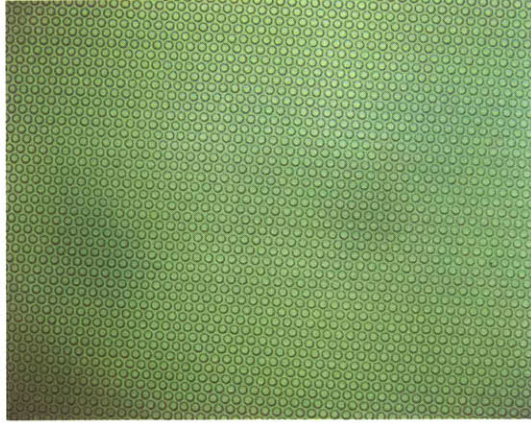


Figure 3.1: An optical microscopy image of a pick-up stamp before pick-up of gold membrane. Each circular air cavity in the PDMS layer is about $12.5\ \mu\text{m}$ in radius, and there is a spacing of at least $5\ \mu\text{m}$ between the perimeters of adjacent cavities.

3.4 Transfer Pad with Raised Mesas

The transfer pad is fabricated by pouring PDMS (Sylgard 184, Dow Corning Co.), mixed in a 10:1 base-to-curing-agent ratio by weight and degassed under vacuum, onto the silanized SU-8 master with parallelogram troughs, in a Petri dish. The PDMS is then cured in an oven at $50\ ^\circ\text{C}$ for 6 hours. The cured PDMS transfer pad is then peeled from the SU-8 master. This transfer pad has raised parallelogram mesa structures that rise above the plane of the PDMS substrate (refer to Figure 3.3). The mesas aid with the patterning and transfer of the gold electrodes because thermal evaporation is a line-of-sight process, and it is not conformal.

After the curing process, the transfer pad is exposed to oxygen plasma (100W, Plasma Preen, Inc.) for 30 seconds, after which a 90 nm thick organic release layer of N,N'-diphenyl-N,N'-bis(3-methylphenyl)-(1,1'-biphenyl)-4,4'-diamine (TPD, Luminescence Technology Co.) and a 140 nm or 150 nm thick layer of gold are deposited in sequence via thermal evaporation [1] onto the transfer pad to define the gold electrodes on the parallelogram mesas of the transfer pad. The thin

gold film, vacuum-evaporated on top of the parallelogram mesas, breaks along the sharp edges of the mesas, hence, defining a gold film in the shape of the parallelogram. Therefore, the raised areas on the transfer pad define, with sub-micron resolution, the shape of the gold electrodes that are lifted-off onto the pick-up stamps because it is the raised areas that come into conformal contact with the pick-up stamp.

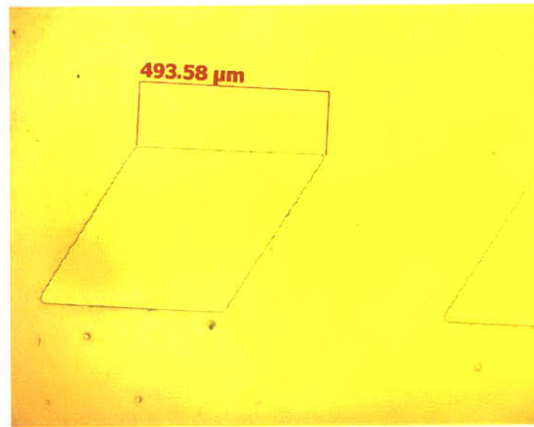


Figure 3.2: An optical microscopy image showing a raised parallelogram PDMS mesa on a PDMS transfer pad, before TPD and gold are evaporated on it. The gold electrode picked-up from this mesa will cover about 256 circular air cavities, each of radius 12.5 μm . The same transfer pad also has bigger parallelogram mesas that have areas that are four times larger than the area of the mesa shown above.

3.5 Contact Lift-Off Transfer

Following the thermal evaporation, the pick-up stamp with circular air cavities is brought into contact with the gold film on the mesas of the transfer pad, and is rapidly lifted-off to peel away and transfer the gold film onto the stamp such that the parallelogram gold films cover the air cavities and form the top electrode of the pressure sensors, as shown in Figure 3.3. Figure 3.4 shows scanning electron micrographs of the SU-8 master mold, the transfer pad parallelogram mesa, the

pick-up stamp, and the transferred gold film. Figure 4.2 shows optical microscopy pictures of one of the devices fabricated using the described process.

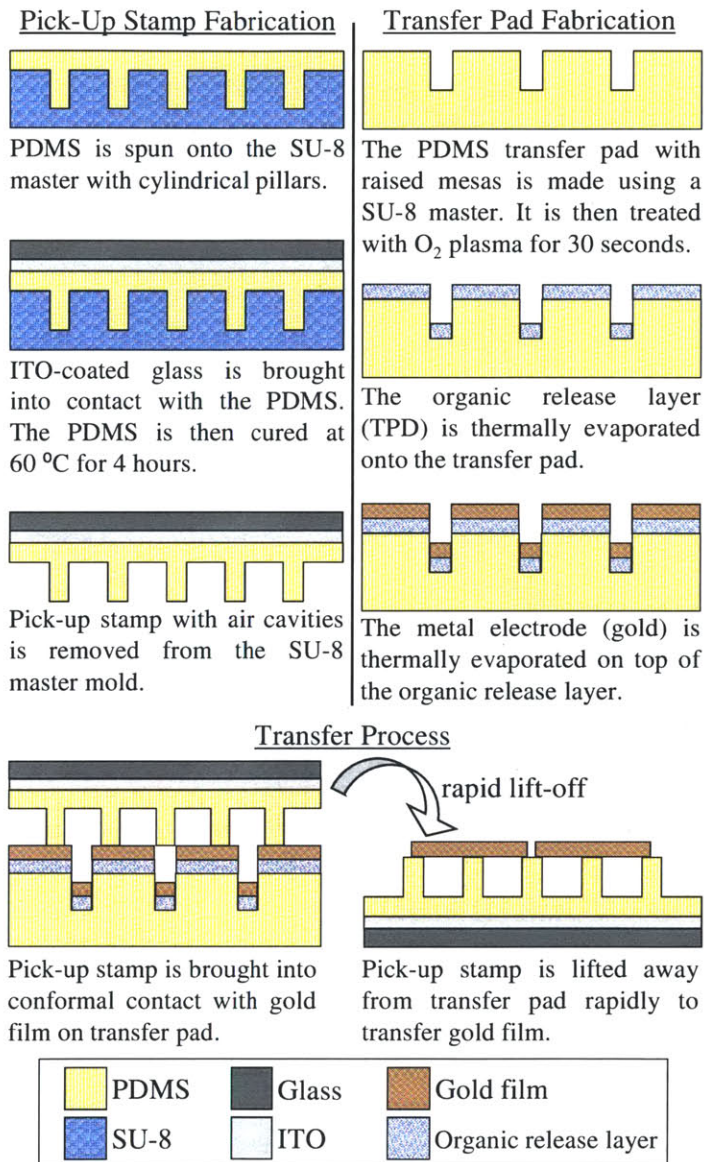


Figure 3.3: The process flow for the contact lift-off mesa-transfer micro-contact printing process. The drawings above are not to scale.

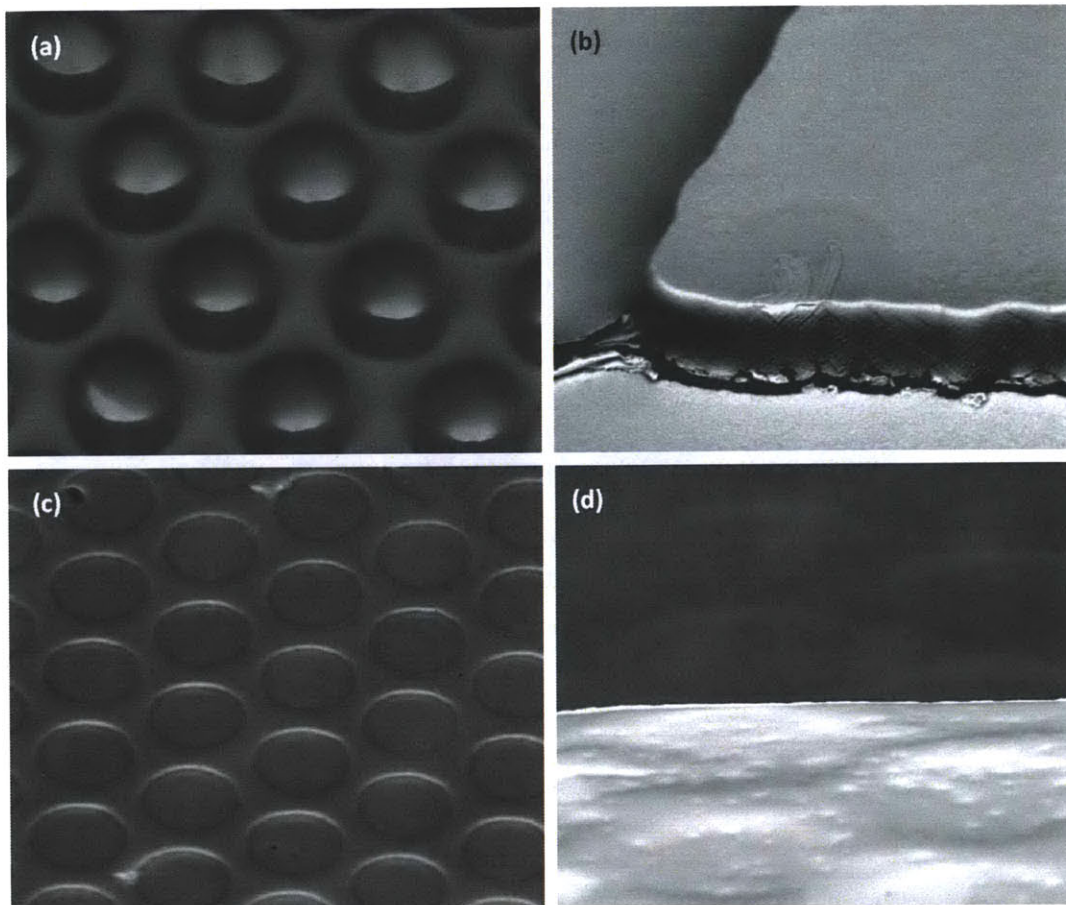


Figure 3.4: Scanning electron micrographs of (a) the SU-8 master mold, (b) a corner of the transfer pad parallelogram mesa with an organic film and a gold film evaporated on top, (c) the cavity-patterned PDMS spacer layer of the pick-up stamp, and (d) the edge of a transferred gold film bridging the air gaps in the PDMS spacer layer of the pick-up stamp.

Chapter 4

PDMS Spacer Layer Device

Characterization

Devices fabricated using the contact lift-off mesa-transfer process described in Chapter 3 have sharper gold film electrode edge definition than the devices fabricated using the shadow-masking process. The mesa-transfer process reduces the edge roughness of the gold electrodes to less than 1 μm , as shown in Figure 4.1. Additionally, the process demonstrates the ability to fabricate electrodes with sharp corners. Figure 4.2 shows a photomicrograph of a pressure sensor with two sharp corners fabricated using the mesa-transfer process.

The mesa-transfer process also has a qualitatively higher device yield than the shadow-masking process. The yield in the mesa-transfer process itself is affected by the depth of the air cavities in the PDMS spacer layer between the gold and the ITO electrodes. Devices with air cavity depths greater than 9 μm have higher yield than devices with cavity depths less than 2 μm , because in the latter devices the gold film comes into contact with, and sticks, to the PDMS at the bottom of the air cavities during the contact-printing step, just before lift-off, hence,

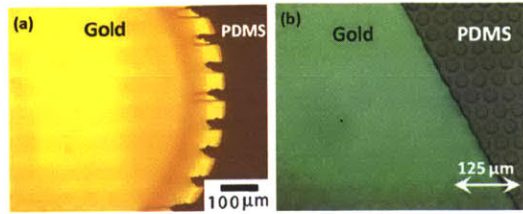


Figure 4.1: Optical microscopy images contrasting the edge definition of devices fabricated using the old shadow-masking process and the new mesa-transfer process. a) Gold electrode of the MEMS device fabricated using shadow-masking. The edges of the electrode have poor definition. b) Gold electrode of the MEMS device fabricated using mesa-transfer. The edges of the electrode are much sharper and have sub-micron edge roughness.

permanently deforming the device.

The electromechanical performance of the fabricated devices is also characterized. The fabricated devices are actuated electrically to demonstrate that the gold membrane above the air cavities can deflect in response to a voltage applied between the gold membrane (the top electrode) and the ITO (the bottom electrode). As the applied voltage increases, the electrostatic force of attraction between the top and bottom electrode increases, causing the gold membrane bridging the air cavity to deflect more and, hence, decrease the distance between the electrodes. The decrease in the distance between the two electrodes results in an increase in the capacitance of the device, allowing mechanical deflection to be sensed electrically. The mechanical deflection of the membrane in response to electrostatic actuation mimics the mechanical deflection of the membrane in response to pneumatic loading. Thus, electrostatic actuation of the device is a convenient method for its electromechanical characterization.

A device comprising a 32×32 array of 1024 air cavities (in PDMS) covered by a single gold electrode, is actuated with an Agilent 4156C Precision Semiconductor Parameter Analyzer to perform quasi-static capacitance-voltage (QSCV) measure-

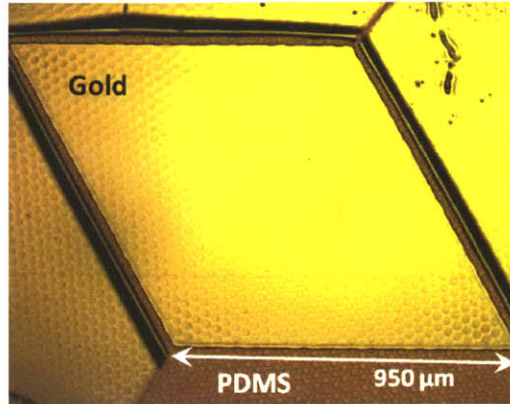


Figure 4.2: An optical microscopy image of the pressure sensor fabricated using the contact lift-off mesa-transfer process. The gold parallelogram is the pressure sensor. Sags are visible in the gold membrane above the circular cavities. About 1024 circular cavities are covered by this parallelogram gold membrane which is about 140 nm thick. The mesa-transfer process enables the printing of sharp corners, with sub-micron edge roughness. The underlying PDMS on ITO-Glass is patterned with 25 μm diameter circular cavities with about 5 μm to 7 μm spacing between the circles. The circular cavities are arranged in a hexagonal-close-packed pattern.

ments. Electrical contact with the device electrodes is made using a compliant probe tip and gold wire. The gold-wire probe tip contacts the gold membrane of the device. The compliant probe tip contacts the ITO layer of the device which is exposed by scratching away some of the PDMS on the pick-up stamp. A voltage is applied between the top and bottom electrodes and increased in steps of 1.0 V. The resulting capacitance of the device is measured as a function of the applied voltage.

The results of the QSCV measurements over three runs on the same device are shown in Figure 4.3. The increase in the capacitance of the device with increasing voltage indirectly demonstrates deflection of the gold membrane, which bows under the electrostatic force to decrease the gap spacing over the air cavities in the PDMS spacer layer, thus increasing the capacitance.

Gold membrane deflection under electrical actuation is viewed from the back of

the device, through the transparent, ITO-coated glass substrate, using an optical microscope. As the voltage is increased, the membrane deflects towards the glass substrate. The membrane pulls in at voltages greater than 90 V, as shown in Figure 4.4.

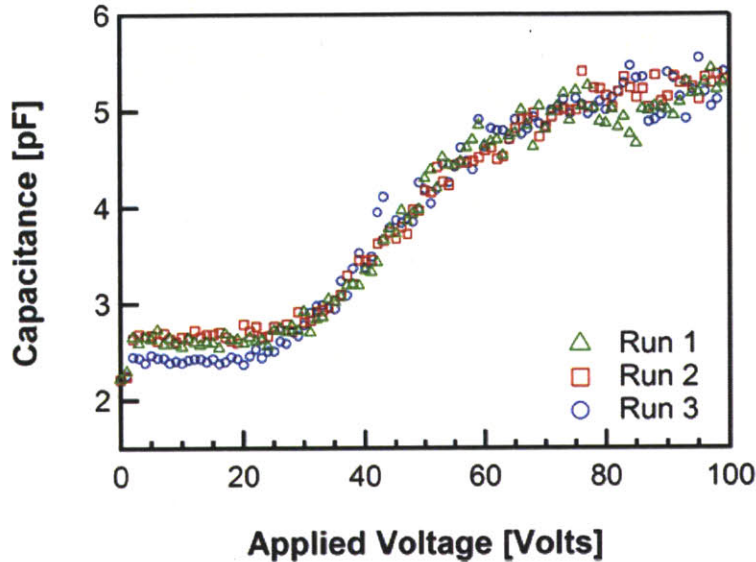


Figure 4.3: Three capacitance-voltage sweeps for a single device. The approximate two-fold increase in the capacitance of the device with voltage indirectly demonstrates deflection of the gold membrane, which bows under the electrostatic force to decrease the gap spacing over the air cavities in the PDMS spacer layer, thus increasing the capacitance.

Profilometry is performed to measure the device dimensions. A contact profilometer is used to measure the depths of the air cavities and the thickness of the residual PDMS layer within the air cavities. The profilometer-measured distance between the top and bottom electrodes (modeled as the parameter d in Chapter 2), is $15.4 \mu\text{m}$ —nearly three times larger than the modeled value. Additionally, the residual PDMS layer is $5.6 \mu\text{m}$ thick—almost twice as large as the modeled value, $t = 3 \mu\text{m}$. Thus, lack of control over the PDMS spacer layer thickness leads to the cavity depth, and the residual PDMS thickness being much greater

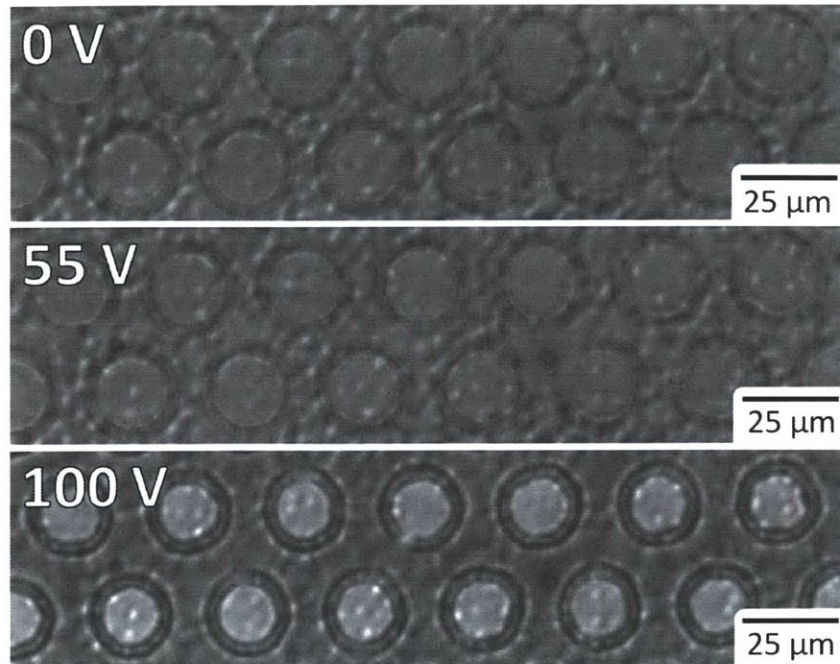


Figure 4.4: Optical microscopy images of gold membrane deflection under electrical actuation, as the voltage applied is increased. The membrane is being imaged from the back of the device, through the transparent, ITO-coated glass substrate. The membrane pulls in at voltages greater than 90 V.

than anticipated. In order to effect the same device capacitance change at lower voltages, the thickness of the PDMS layer, d , needs to be decreased by decreasing the thickness of the SU-8 resist used to make the SU-8 master. The thickness, t , of the residual PDMS layer in the cavities also needs to be decreased in order to increase the device capacitance change at lower voltages.

Chapter 5

Contact-Transfer Printed MEMS

Membranes on Silicon Dioxide

The aforementioned capacitive MEMS devices fabricated by contact-printing 140 nm thick gold membranes onto patterned polydimethylsiloxane (PDMS) substrates suffer from high actuation voltages and minimal membrane deflection under bias, due to difficulty in controlling the thickness of the PDMS dielectric layer. Additionally, a viscoelastic spacer layer between the top and bottom electrodes lacks robustness and is susceptible to ambient parameters. Therefore, it is worthwhile to explore the contact-printing of metal electrodes on materials such as silicon and silicon dioxide because the thickness of dielectric spacer layers of these materials can be precisely controlled, down to the sub-micron regime. Decreasing the spacer layer thickness can enable the low power operation of contact-printed sensors and actuators. Moreover, the ability to contact-print suspended metal membranes directly onto silicon-based substrates will enable this contact-printing technology to complement existing integrated-circuit fabrication technologies to effect low-cost fabrication of large-area arrays of MEMS devices. Furthermore,

silicon and silicon-based spacer layers are more stable and less porous than viscoelastic PDMS spacer layers. This could potentially enhance the lifetime of the printed MEMS devices.

5.1 Prior Work and State of the Art

The adhesion of gold films to silicon or silicon dioxide is observed to be significantly weaker than that of gold films to PDMS. The contact-printing approach discussed in prior chapters failed to effect repeatable transfer of gold films onto patterned silicon dioxide surfaces without any modifications to the process. A variety of thin-film transfer methods from literature were also considered. However, most of these methods demonstrated the transfer of metallic films with thicknesses less than 100 nm, and onto planar substrates without any patterned cavities or gaps. The efficacy of chemical-bonding aided transfer methods is significantly reduced when the receiving substrate is extensively patterned with recessed gaps or cavities for MEMS applications. This is because patterning of the substrate considerably reduces the effective surface area of the substrate available for chemical bonding with the metallic film on the transfer pad. A substrate with hexagonal close packed, 25- μm -diameter circular cavities with 30 μm center-to-center distance, as discussed in the preceding chapters, has an effective bonding surface area that is 64% less than that of a planar, non-patterned substrate.

Covalent-bonding-aided additive transfer of 25 nm thick, non-deflectable metal films onto non-patterned silicon substrates was demonstrated by Loo et al. [8]. In that study, the transferred gold films were only 20 nm thick, and were coated with a 5 nm thick titanium layer to enable covalent bonding between the film and the substrate via a condensation reaction between the oxide-forming titanium layer

and the silicon-based substrate, such as PDMS or plain silicon. Additionally, these membranes were transferred onto planar, non-patterned, rigid and flexible substrates and, as a result, deflection of these membranes was not reported.

Metal films have also been selectively lifted-off to pattern cathodes for organic light-emitting devices via cold welding [9]. A patterned silicon stamp is coated with a 5 nm thick chromium layer, followed by a 15 nm thick silver layer. This stamp is brought into conformal contact with a 50 nm thick Mg:Ag alloy cathode (deposited atop a stack of organic layers) covered with a 40 nm thick silver layer. 290 MPa of pressure is applied to ensure conformal contact between the cathode layer and the metal layer (on the stamp), and to assist in the formation of a metallic junction between the two atomically flat surfaces. The stamp is then lifted-off to remove metal from the cathode layer in areas of conformal contact with the stamp, hence patterning the cathode layer. Cold welding has yet to be used to demonstrate the fabrication of suspended metal membranes for MEMS applications.

5.2 The Acetone-Assisted Contact-Transfer MEMS Fabrication Process

As discussed in the preceding section, it is difficult to transfer ~100 nm thick gold films from a transfer pad onto a cavity-patterned silicon or silicon-dioxide spacer layer, even after the chemical modification of the spacer layer surface via silanization with thiols. Hence, in addition to spacer layer surface silanization, the contact-printing process discussed in the preceding chapters is modified by using acetone to dissolve the underlying organic (TPD) film on the transfer pad

to effect the repeatable transfer of gold films from the transfer pad onto a cavity-patterned silicon dioxide spacer layer. This novel acetone-assisted contact-transfer method successfully transfers 110 nm to 140 nm thick gold films onto patterned silicon dioxide dielectric spacer layers to form MEMS capacitors. This method enables finer control of the dielectric layer thickness, and reduces it to 400 nm for the initial demonstration. Additionally, repeatable maximum deflection of the printed membranes is increased six fold, to ~ 150 nm, at 15 V actuation, which is about a third of the voltage reported for the PDMS spacer layer devices of similar geometries [1].

5.2.1 Device Design

The device structure consists of circular cavities in a silicon dioxide dielectric layer that sits atop a doped silicon substrate. The cavities are bridged by a gold membrane that forms the deflectable top electrode. Complying with the contact-transfer process limits, the area of the deflecting membrane is reduced to a circular region of $27 \mu\text{m}$ diameter. Additionally, in order to produce a detectable sound pressure level under actuation, many such deflectable regions are combined in parallel, by printing a large gold electrode that covers about 1000 cavities. These cavities are arranged in a hexagonal-close-packed pattern to minimize the non-active capacitance from the silicon dioxide supports. Hence, the gold electrode is parallelogram-shaped to maximize the number of cavities covered for any given area. Moreover, the large gold electrode serves to demonstrate the ability to fabricate large membranes. The variable capacitance MEMS structure can be used to produce sounds or sense pressure as the gold membrane of the structure deflects in response to applied voltage or applied pressure.

5.2.2 Pick-up Stamp Substrates

The pick-up stamp is fabricated by cleaning a doped silicon wafer in Piranha solution. This wafer forms the back electrode of the device. A 400 nm thick silicon dioxide layer is deposited on the wafer using plasma-enhanced chemical vapor deposition (PECVD). Hexamethyldisilazane is then applied to the oxide layer. Photoresist is spun on the oxide layer and pre-baked at 90°C for 35 minutes. The photoresist is then exposed to UV light in a mask aligner and exposure unit, using a transparency mask. Following exposure, the photoresist is developed and dried. The resulting photoresist layer has circular patterns, with the underlying SiO₂ exposed; see Figure 5.1. The exposed SiO₂ is dry etched in tetrafluoromethane (CF₄) in a reactive ion etcher, forming circular cavities, about 27 μm in diameter. A thin layer (~30 nm) of SiO₂ is not etched in the cavities to provide an insulating layer between the gold membrane and the bottom electrode. The photoresist is ashed in O₂ in the reactive ion etcher as well.

The wafer is cleaned using acetone, and then in a basic Piranha solution (1:1:3, NH₄OH:H₂O₂:H₂O) for 45 minutes to make the patterned silicon dioxide surface hydrophilic for silanization. After the Piranha clean, the wafer is rinsed with deionized water, blown dry using nitrogen, and cleaved into smaller slides, approximately 1 cm² in area. These slides are then placed in a 0.001:1 (by volume) solution of 3-mercaptopropyltrimethoxysilane (Sigma-Aldrich) and ethanol at 80 °C for 24 hours to silanize the silicon dioxide surface such that thiol groups stick out of the oxide surface, enhancing the adhesion of gold to the oxide. Upon silanization, these pick-up stamp slides are sonicated in isopropanol for 5 minutes, and then blown dry using nitrogen, immediately prior to the transfer step. A contact profilometry scan of the cavity-patterned silicon dioxide pick-up stamp

is shown in Figure 5.2.

5.2.3 Transfer Pad with Raised Mesas

The transfer pad fabrication for the acetone-assisted contact-transfer process is similar to that for the PDMS spacer layer device fabrication. It is listed here with appropriate parameter modifications for completeness. The master mold that defines the transfer pad geometry is fabricated using SU-8 photoresist. The photoresist is spun onto a clean silicon wafer. The wafer is then pre-baked on a hot plate at 95 °C for 5 minutes. Next, the wafer is cooled for 2 minutes before being placed in a UV exposure unit with a transparency mask on top of the photoresist layer, with the mask emulsion in contact with the photoresist. The photoresist is exposed to UV light, after which, the wafer is baked at 95 °C for 2 minutes. The photoresist is developed by immersing the wafer in propylene glycol monomethyl ether acetate (PGMEA) for 4 minutes and agitating. Next, the wafer is sprayed with PGMEA and isopropanol in sequence, for 10 seconds each, to rinse off residual SU-8 and PGMEA, respectively. The wafer is blown dry with nitrogen and hard-baked for 3 hours at 150 °C on a hot plate. Following the hard bake, the SU-8 mold is silanized with trichloro(1H,1H,2H,2H-perfluorooctyl)silane (Sigma-Aldrich) to ensure easy removal of the cured PDMS [1], thus completing the reusable-master-mold fabrication.

The transfer pad fabrication begins by mixing PDMS (Sylgard 184, Dow Corning Co.), in a 10:1 base-to-curing-agent ratio by weight, and degassing it under vacuum. The PDMS is then poured onto the silanized SU-8 master in a Petri dish, and cured in an oven at 60 °C to 70 °C for 6 hours. The cured PDMS pad is peeled from the SU-8 master. This pad has parallelogram-shaped mesa struc-

tures that rise above the plane of the PDMS substrate and aid the patterning and transfer of the metal electrodes since thermal evaporation is a line-of-sight process; see Figure 5.1. After curing, the PDMS transfer pad is exposed to oxygen plasma for 35 seconds, after which a 70-90 nm thick organic release layer of N,N'-diphenyl-N,N'-bis(3-methylphenyl)-(1,1'-biphenyl)-4,4'-diamine (TPD, Luminescence Technology Co.), and a 110-140 nm thick layer of gold are deposited in sequence via thermal evaporation onto the transfer pad to define the gold electrodes on the mesas of the transfer pad [11]. Since the gold film vacuum-evaporated on top of the parallelogram mesas is much thinner than the height of the mesas, it breaks along the sharp edges of the mesas, defining a gold film in the shape of the mesas with sub-micron resolution. This gold film is then lifted-off onto the pick-up stamps due to conformal contact between the raised mesas and the pick-up stamps during the transfer process.

5.2.4 Contact Lift-Off Transfer

To initiate the gold membrane transfer following the thermal evaporation, 50 μL of acetone is applied to a $\sim 1 \text{ cm}^2$ area on the transfer pad to dissolve the TPD layer underneath the parallelogram-shaped gold membranes. Most of the dispensed acetone is allowed to evaporate. The pick-up stamp is then placed in contact with the gold membranes, which are still resting on the mesas of the transfer pad, but which now adhere to the MPTMS treated pick-up stamp, and are lifted-off. The transferred parallelogram-shaped gold membranes with sub-micron edge definition cover the circular air-cavities in the stamp, forming the top electrode of the MEMS device, as shown in Figure 6.1.

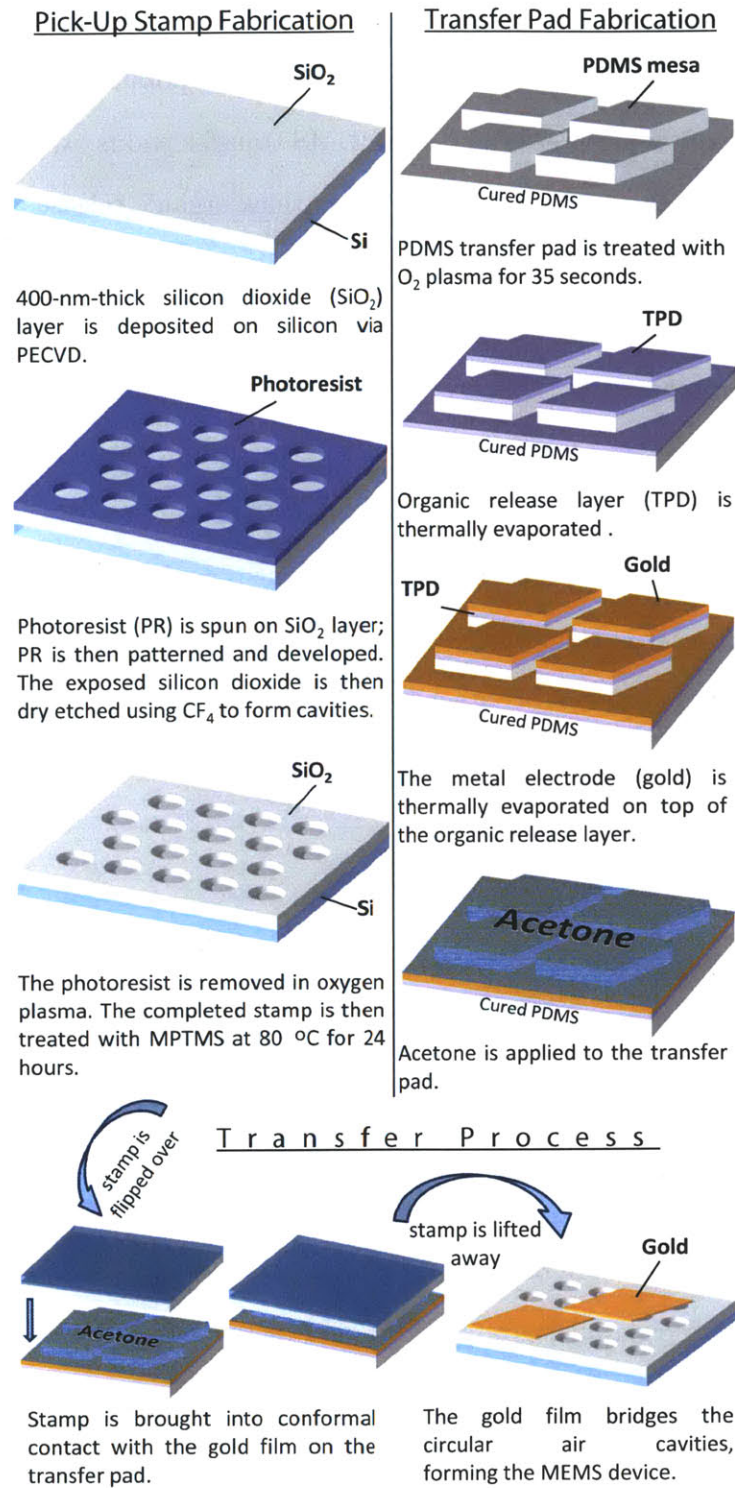


Figure 5.1: The process flow for the acetone-assisted, contact-transfer MEMS printing process on silicon-based substrates. The drawings above are not to scale.

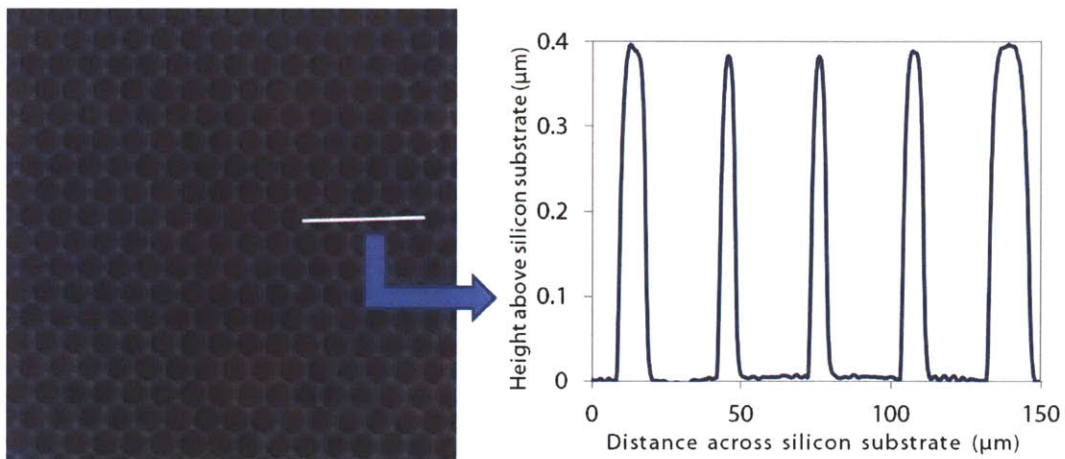


Figure 5.2: A contact profilometry scan of the pick-up stamp. The pick-up stamp consists of a 400 nm thick silicon dioxide spacer layer on a silicon substrate. The silicon dioxide spacer layer is patterned with circular cavities in a hexagonal-close-packed arrangement.

Chapter 6

Silicon Dioxide Spacer Layer Device Characterization

The ability of an area of gold membrane transferred onto a patterned silicon dioxide surface to function as an acoustic MEMS device depends on the number of cavities covered by the gold membrane over which the membrane has not sunk in permanently due to the fabrication process. Application of excessive pressure during the contact-transfer process results in the gold membrane over some cavities coming into contact with the bottom of those cavities, and sticking to it, perhaps due to the presence of MPTMS in the cavity wells or due to acetone-enabled stiction. Devices in which 0% to ~90% of the gold-covered cavities are functional have been fabricated repeatedly via this process. It is expected that the yield of the process increases with the thickness of the silicon dioxide spacer layer, as noticed with the PDMS spacer-layer devices [11].

The electromechanical performance of the device membranes is characterized via optical interferometry. The fabricated devices are electrically actuated using a gold-wire probe tip to contact the gold membranes of the devices. As the voltage

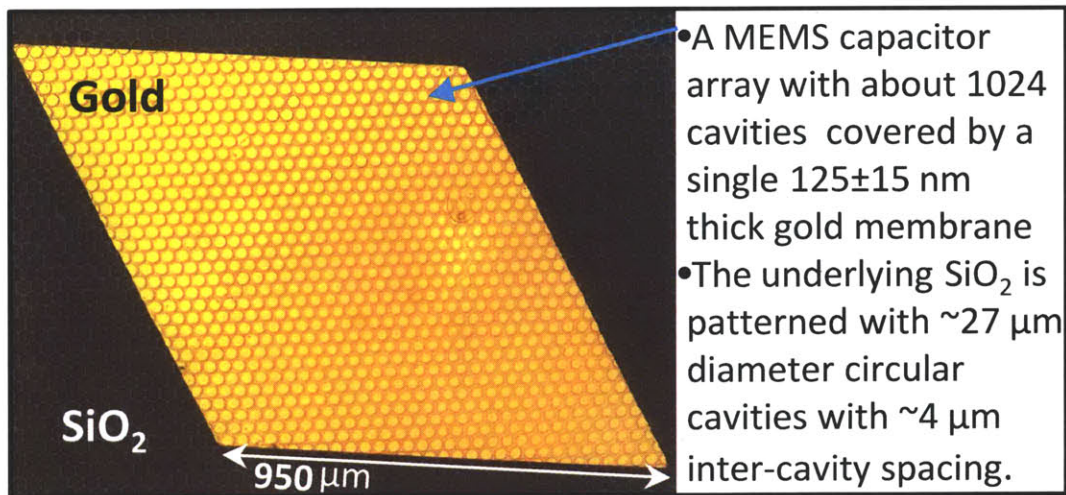


Figure 6.1: Optical microscopy image of a $\sim 0.8\text{mm}^2$ area gold membrane MEMS device printed on silicon dioxide using the acetone-assisted contact-transfer process.

applied between the gold membrane (the top electrode) and the silicon substrate (the bottom electrode) is varied, the resulting deflection of the membranes is profiled using an optical interferometer (Wyko NT9100, Bruker Nano Inc.). As the applied voltage increases, the electrostatic force of attraction between the flexible top electrode and the rigid bottom electrode increases, causing the gold membrane suspended over the air cavity to deflect more, as shown in Figure 6.2. As the voltage increases from 1 V to 5 V, the deflection is small. The deflection becomes much larger as the voltage increases beyond 6 V. The maximum deflection of a 125 ± 15 nm thick gold membrane over circular cavities, each about $27\ \mu\text{m}$ in diameter, is approximately 150 nm at 15 V, for most cavities, as shown in Figure 6.4. Maximum deflection of 200 nm has also been observed for 125 ± 15 nm thick membranes over some cavities, as shown in Figure 6.2c. Membrane deflection is not uniform over all of the cavities, as shown in Figure 7.9. At any particular voltage, the deflection of the membrane is smaller over cavities adjacent to other cavities over which the membrane has sunk in permanently due to the fabrication

process. This could be due to the fact that when a gold membrane sinks into a cavity and sticks to the cavity walls during fabrication, it is stretched beyond its elastic limit, and in turn, the resulting strain produces tension in the gold membrane over the adjacent cavities, as discussed in Chapter 7, Section 2. This tension opposes the motion of the membrane due to the electrostatic force when a voltage bias is applied, hence, decreasing the deflection of the membrane over the surrounding cavities at that applied bias.

The deflection profiles in Figure 6.2a are single interferometry measurements, resulting in noisy deflection profiles. However, 13 different diametrical deflection profiles of a membrane over a single cavity under 15 V actuation are plotted and averaged to show the mean deflection profile in Figure 6.2b. The averaging of the deflection profiles reduces the measurement noise from the optical interferometer. Additionally, a 15 Hz sinusoidally-varying voltage of 15 V peak-to-peak amplitude is applied to the device to demonstrate that this large maximum membrane deflection is a repeatable deflection, as shown in Figure 6.3.

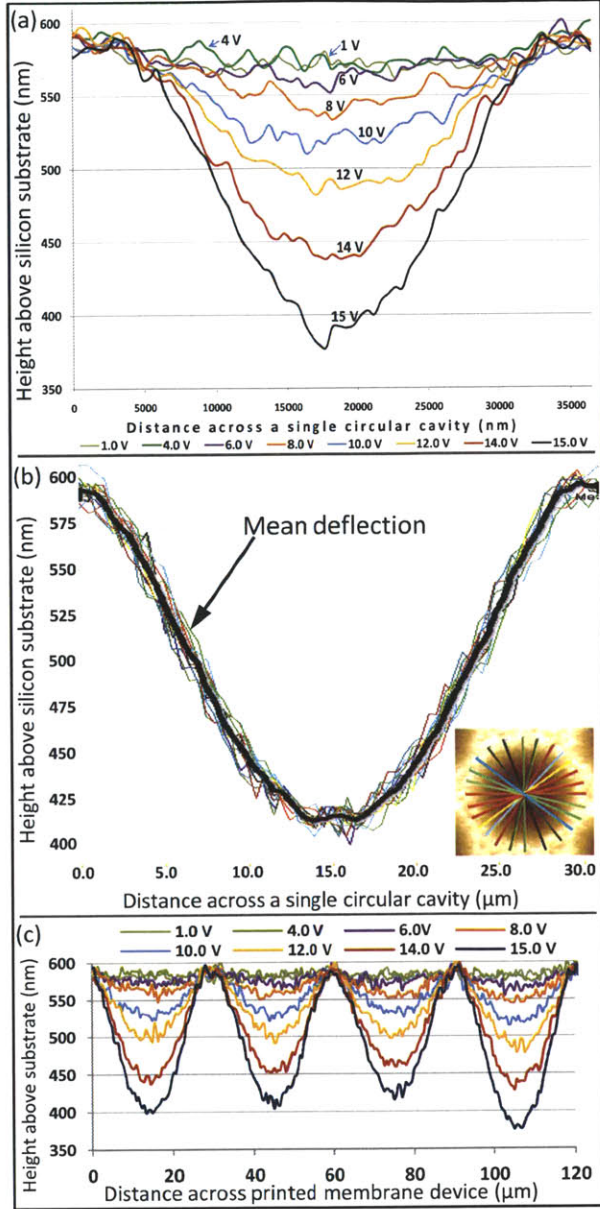


Figure 6.2: Deflection profiles of gold membranes under electrostatic actuation, obtained via optical interferometry. The height values shown above are offset by about 60 nm due to the presence of transparent oxide in the cavity reference region used by the interferometer. The deflection values, however, are absolute, i.e., about 60 nm should be subtracted from each point on each deflection curve above. (a) Deflection of the membrane increases as the voltage applied between the membrane and the Si substrate increases. (b) 13 different diametrical deflection profiles (inset: interferometry image) of a membrane under 15 V actuation, are plotted and averaged to show the mean profile. (c) Gold membrane deflection over multiple cavities covered by a single membrane, as the voltage is increased from 1 V to 15 V.

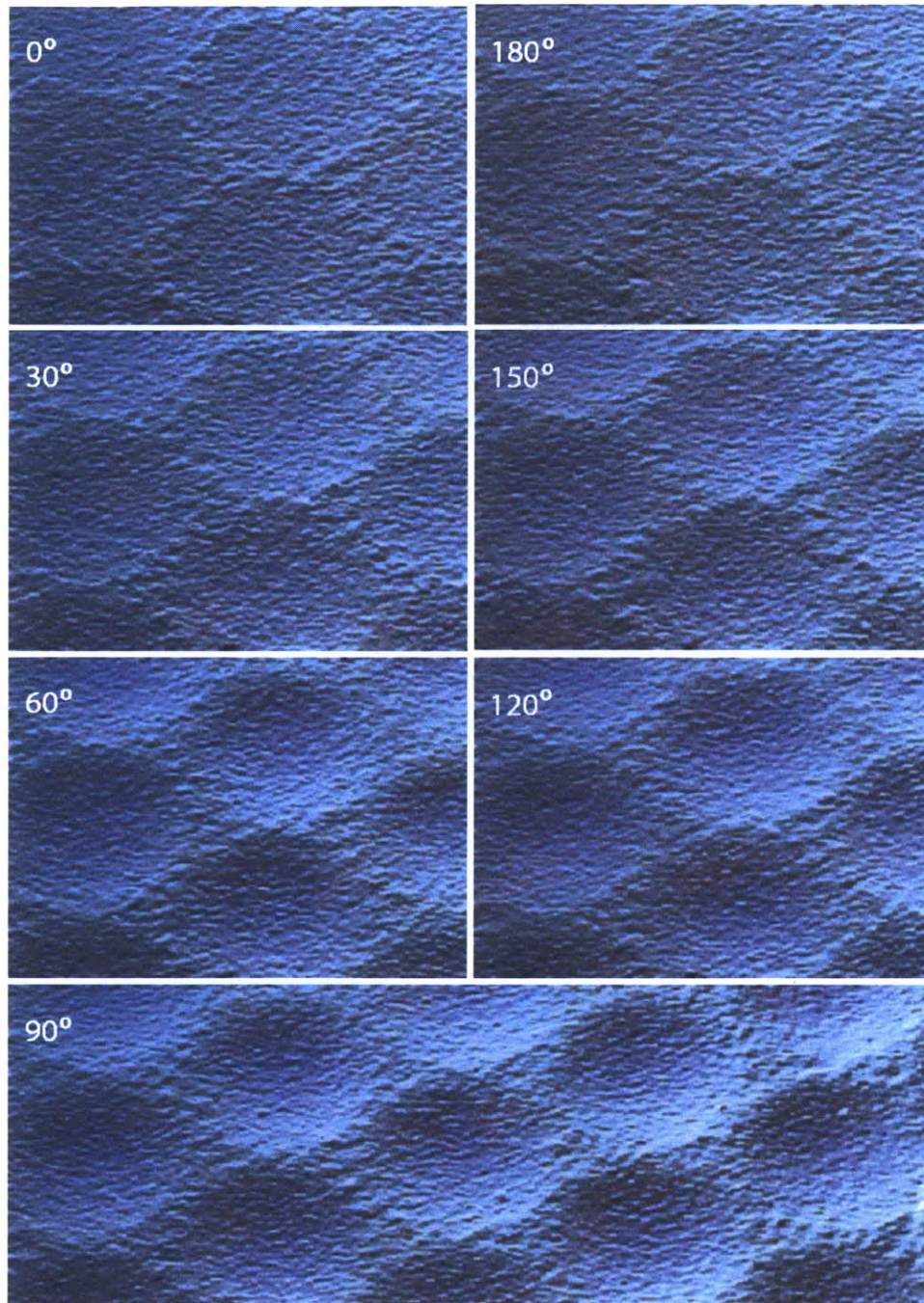


Figure 6.3: Optical interferometry images of several cavities under 15 V peak-to-peak amplitude sinusoidal voltage actuation at 15 Hz, taken at 30° phase intervals. Membrane deflection for only one half of a sine wave is shown in this figure. Each cavity is about $27\ \mu\text{m}$ in diameter.

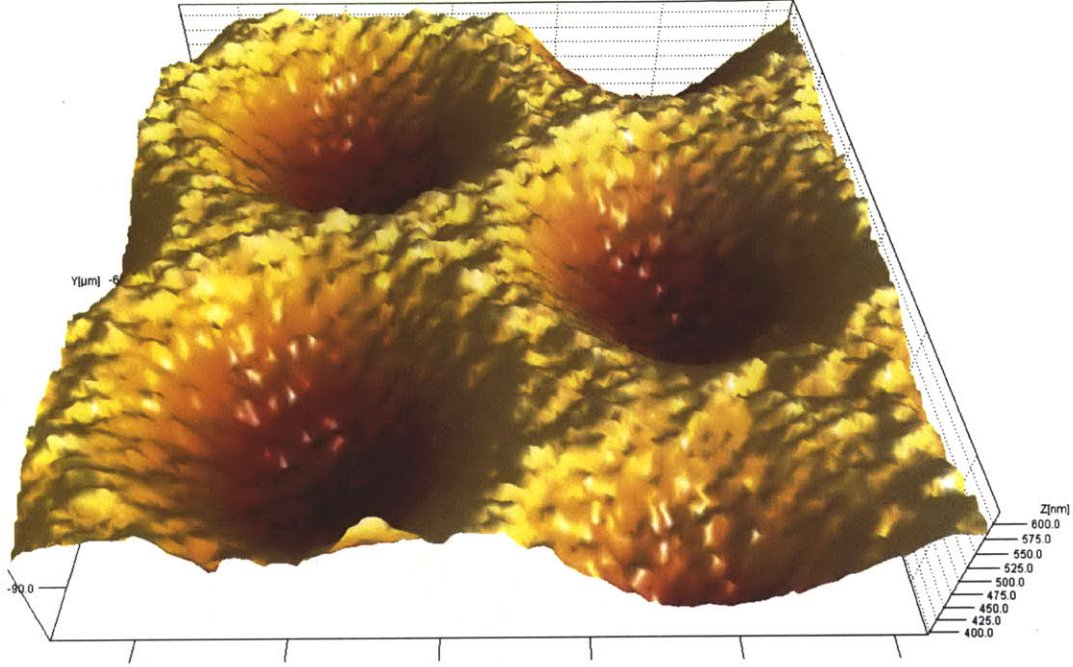


Figure 6.4: A 3-D image of a gold film deflected over circular cavities, obtained using optical interferometry. The maximum deflection of the gold film is about 150 nm in the center, under 15 V bias. The diameter of each circular cavity is about 27 μm .

6.1 Analysis

6.1.1 Determining Young's Modulus

The membranes have a repeatable maximum deflection, w_0 , that usually exceeds the thickness, h , of the membranes over the range of applied mechanical pressures or voltages, as shown in Figure 6.2a. Therefore, the theory of bending of plates that is valid for deflections much smaller than the thickness of the plates is inapplicable here. Instead, gold membrane deflection is modeled by using the energy method, as outlined in [7]. We assume that the shape of the deflected membrane can be modeled by a profile, $w(r)$, that is obtained by applying a spatially-uniform pressure, where

$$w(r) = w_0 \left(1 - \frac{r^2}{a^2}\right)^2 ; \quad (6.1)$$

r is the radial distance from the center of the cavity of radius a , and w is the deflection of the membrane at r . Figure 6.5 shows the fit of the deflected membrane profile, obtained via interferometry at 15 V applied bias (from Figure 6.2a) to Equation 6.1. This good fit implies that the radially-varying electric pressure can be approximated as an effective uniform pressure which, in turn, is used to calculate the Young's modulus, E , of the gold membrane. Assuming a 30 nm thick SiO₂ dielectric insulating layer in the cavity, for a 125±15 nm thick gold membrane, E is 74±17 GPa. The uncertainty in the derived value of E comes from measurement uncertainty in h , and, hence, in h^{-3} . The Young's modulus of gold often quoted in literature is 79 GPa.

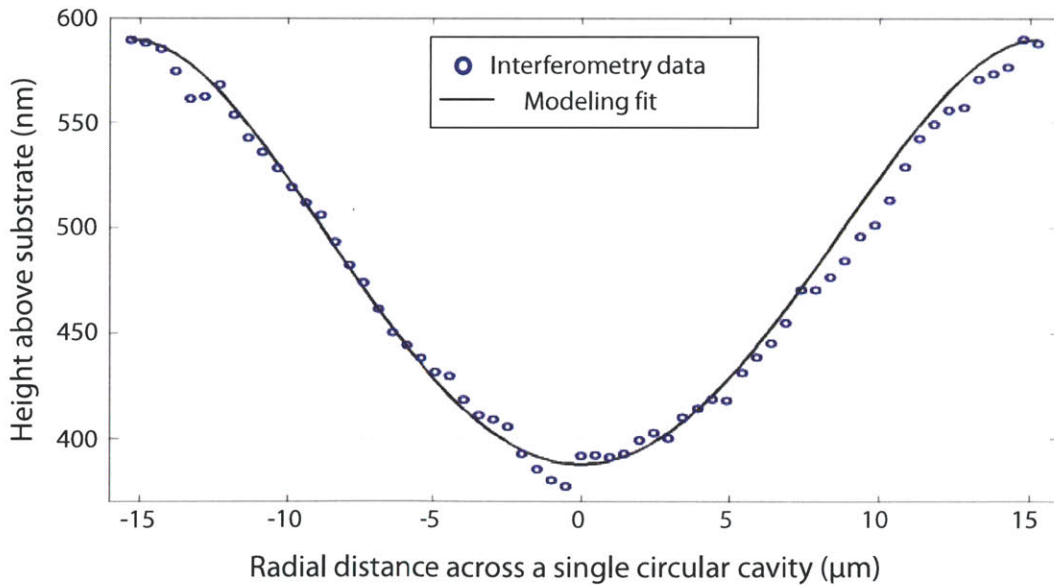


Figure 6.5: Equation 6.1 fitted to the profile of a deflected membrane at 15 V bias, obtained via optical interferometry.

6.1.2 Potential Sound Pressure Level Output

One possible application of the MEMS device fabricated above is microspeakers for earphones and hearing aids. Its acoustic response or sound pressure level (SPL) is modeled by assuming that the dimension of the device and the ear cavity is smaller than the wavelength of sound at audible frequencies. This results in the sound pressure produced by the device being distributed uniformly in the ear cavity. Thus, the SPL generated by the device is given by [12]:

$$SPL = 20 \log_{10} \left(\frac{1.4 P_0 |\Delta V|}{P_{ref} V_0} \right) \text{ (dB)}, \quad (6.2)$$

where P_0 is the atmospheric pressure, $P_{ref} = 20 \text{ }\mu\text{Pa}$, $V_0 = 2 \text{ cm}^3$ is ear cavity volume, and $|\Delta V|$ is the volume of air displaced by the deflecting membrane. Therefore, the greater the membrane deflection, the higher the SPL generated. For a 0.8 mm^2 device (as shown in Figure 6.1) with 1024 functional cavities in a 400 nm thick SiO_2 spacer layer, we estimate the generated SPL to be approximately 45 dB, assuming 15 V operation and using the deflection profile in Figure 6.2a to calculate the volume of air displaced, $|\Delta V|$. Instead, if uniform deflection of the membrane (150 nm) is assumed, then the expected SPL estimate is 52 dB—but this estimate probably has a larger error due to the parallel-plate deflection profile assumption. Earphones need to produce a minimum of 90 dB SPL, which can potentially be achieved with a $\sim 135 \text{ mm}^2$ gold membrane printed on a 400 nm thick silicon dioxide spacer layer, and actuated at 15 V. The SPL generated can be increased by increasing the cavity diameter, and by increasing the transferred membrane area. Fortunately, the membrane area required to produce any given SPL decreases with increasing voltage. Moreover, the pull-in voltage of these devices can be increased by increasing the silicon dioxide spacer layer thickness.

This increases the cavity depth, and hence increases the distance the membranes can deflect before pulling in, resulting in a higher SPL production. However, this implies higher operating voltages, as demonstrated in Chapter 8.

Chapter 7

Quality of Contact-Printed Films on Silicon-based Substrates

7.1 Surface Roughness of Transferred Gold Films

The surface roughness of gold membranes transferred via acetone-assisted contact-transfer printing is investigated via optical interferometry. 125 ± 15 nm thick gold films are transferred on to planar silicon substrates without any patterned features. Prior to film transfer, the silicon substrates are cleaned using the substrate-cleaning procedure outlined in Chapter 3, Section 3. Gold films are contact-printed onto the planar substrates using the contact-transfer printing process with modified parameters, as outlined in Chapter 8. Most of the transferred gold films are wrinkle-free, and they lie parallel to the substrate onto which they are transferred. However, some of the transferred gold films exhibit wrinkling due to the out-of-plane folding of these films, during the transfer step. These films could be wrinkling due to the non-uniformity of the pressure applied prior to the lift-off step. Currently, the entire process of acetone application, pressure application,

and lift-off is being done manually. Uniform transfer of planar films without wrinkling could potentially be achieved using a tool that applies uniform pressure across the entire substrate simultaneously, prior to lift-off. The successful transfer of films onto planar, unpatterned substrates also confirms that the transfer of gold films onto silicon-based substrates, both patterned and unpatterned, is not due to the entrapment of acetone in the cavities.

An optical interferometer (Wyko NT9100, Bruker Nano Inc.) is used to obtain the surface profile of the transferred films, at varying magnifications, for different regions on the films. The interferometer outputs an average of nine scans for each region. The number of scans to average is specified by the user, and the averaging of scans reduces the noise in the measurement due to the interferometer apparatus itself.

A $630\ \mu\text{m} \times 473\ \mu\text{m}$ region of a gold film transferred onto a planar silicon substrate, without any tilt correction, has an average surface roughness of 9.24 nm and a root mean square roughness of 11.45 nm, as shown in Figure 7.1. The average surface roughness of the same region decreases to 1.94 nm, and the root mean square roughness decreases to 3.03 nm when tilt correction is applied, as shown in Figure 7.2. Tilt correction enables more accurate values of film surface roughness to be obtained because the error in absolute height values of the gold film surface due to interferometer stage tilt, or due to any substrate unevenness, is reduced.

The interferometer image in Figure 7.2 shows that the roughness of the transferred film increases due to the presence of micron-sized ‘specks’ on the film, each about 50-60 nm in height. These specks are distributed throughout the film and they could be residue from acetone processing prior to the lift off step. When acetone is added to the transfer pad, it dissolves the organic TPD layer underneath

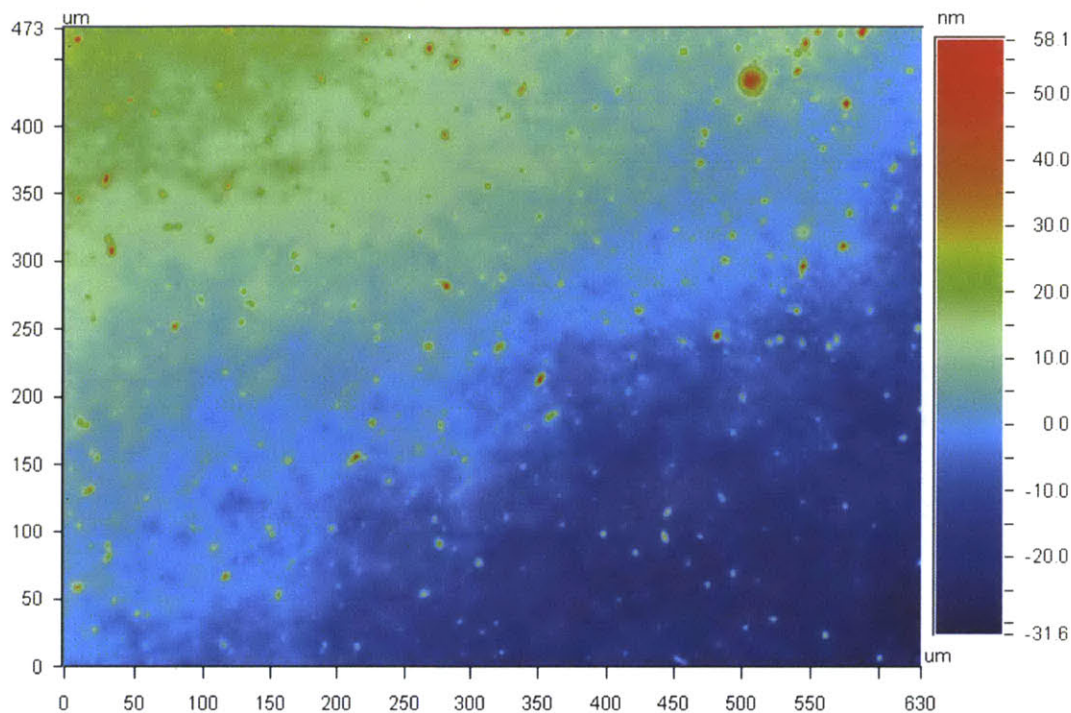


Figure 7.1: An optical interferometry image of a $630\ \mu\text{m} \times 473\ \mu\text{m}$ region of a gold film transferred onto a planar silicon substrate, without any tilt correction. This region of the transferred film has an average surface roughness of $9.24\ \text{nm}$ and a root mean square roughness of $11.45\ \text{nm}$.

the gold film on the transfer pad. It is possible that as the acetone evaporates, the dissolved TPD crystallizes as several tiny crystals underneath the gold film, and some of these TPD crystals are then transferred along with the gold film, resulting in the specks seen in the interferometer image.

It is also possible that the specks in the interferometer image are due to the dust particles that have accumulated on the transferred film surface over time. The interferometer images in Figures 7.1, 7.2, and 7.3 were taken 77 days after the film had been deposited and transferred. Additionally, it can be speculated that the substrate cleaning procedure outlined in Chapter 3, Section 3, is inadequate, and that it results in films being transferred onto substrates with dust particles.

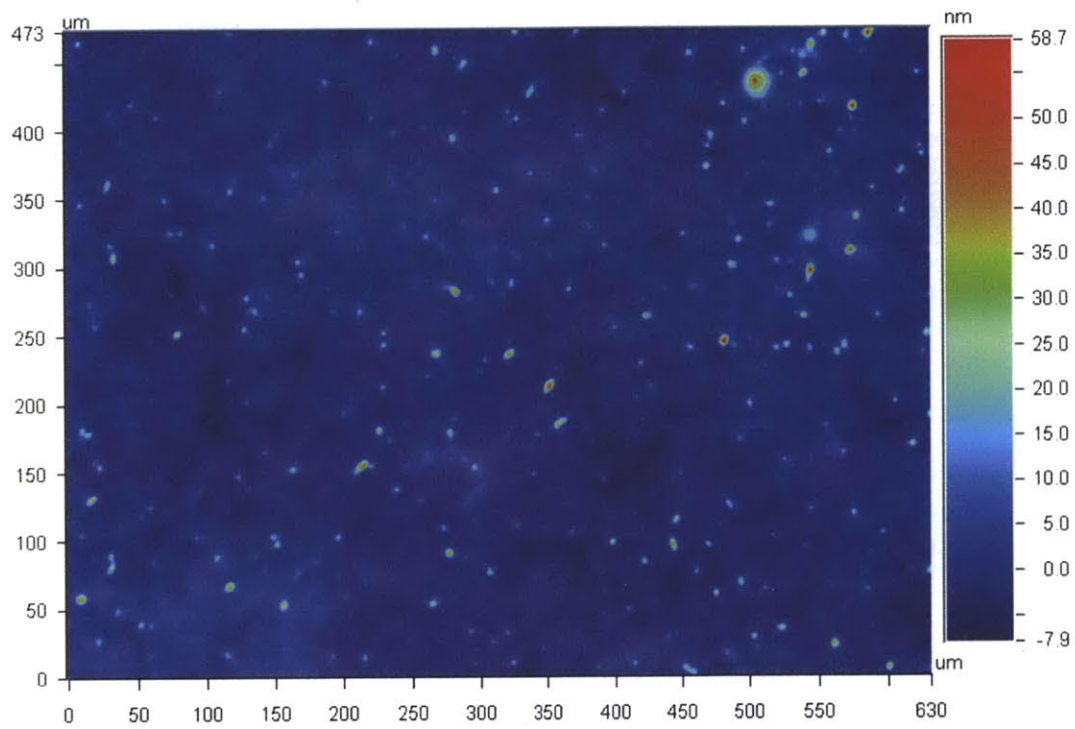


Figure 7.2: An optical interferometry image of a $630 \mu\text{m} \times 473 \mu\text{m}$ region of a gold film (as shown in Figure 7.1), with tilt correction applied. The average surface roughness of the same region decreases to 1.94 nm, and the root mean square roughness decreases to 3.03 nm when tilt correction is applied.

The transferred 125 nm thick gold film then ends up following the uneven surface of the substrate due to the presence of these particles, resulting in the measured roughness.

An area of a transferred gold film about 3.5 times larger ($1.2 \text{ mm} \times 0.87 \text{ mm}$) than the one shown in Figure 7.2, has a slightly larger average surface roughness of 2.27 nm and a larger root mean square roughness of 3.61 nm, as shown in Figure 7.3a. The average surface roughness of the transferred film decreases to 1.32 nm and the root mean square roughness decreases to 1.60 nm when a $50 \mu\text{m} \times 48 \mu\text{m}$ large, speck-free region is examined, as shown in Figure 7.3d. Therefore, contact-transfer printing enables the transfer of large area, near-atomically-flat gold films with relative ease, for a variety of applications.

7.2 Defects in Gold Films Transferred onto Cavity-Patterned Substrates

Gold films transferred via contact-transfer printing onto silicon-based substrates with cavity-patterned silicon dioxide spacer layers, are not defect-free. Two main types of defects are observed, as shown in Figure 7.4. The analysis of these defects is done on a $125 \pm 15 \text{ nm}$ thick gold film transferred over $\sim 1 \mu\text{m}$ deep cavities in a silicon dioxide spacer layer on a silicon substrate.

7.2.1 Irreversible Stiction of Gold Films to Cavity Sidewalls and Cavity Bottom

The transferred gold film sinks into, and sticks to the cavity walls, over some of the cavities in the spacer layer, during the transfer process. This process is

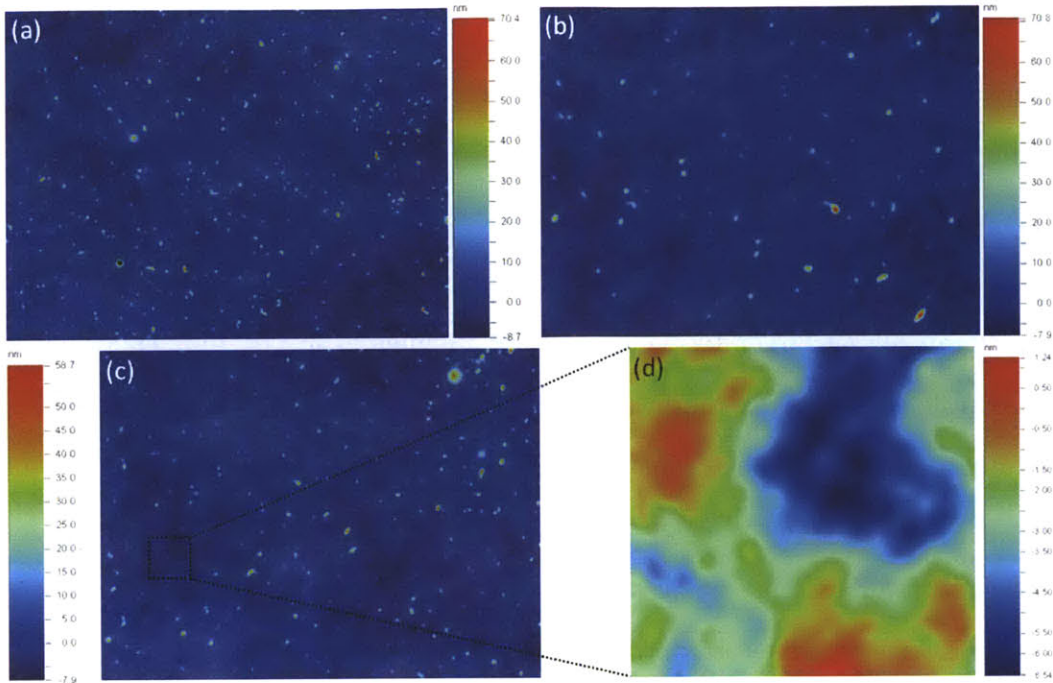


Figure 7.3: Optical interferometry images of the same transferred gold film taken at different magnifications. (a) A $1.2 \text{ mm} \times 0.87 \text{ mm}$ region of a transferred gold film with an average surface roughness of 2.27 nm and a root mean square roughness of 3.61 nm . (b) A $319 \text{ }\mu\text{m} \times 239 \text{ }\mu\text{m}$ region of the same film with an average surface roughness of 1.81 nm and a root mean square roughness of 3.03 nm . (c) A $630 \text{ }\mu\text{m} \times 473 \text{ }\mu\text{m}$ region of the same transferred gold film with an average surface roughness of 1.94 nm and a root mean square roughness of 3.03 nm , as shown in Figure 7.2 also. (d) A $50 \text{ }\mu\text{m} \times 48 \text{ }\mu\text{m}$ subregion of the film in (c) that is largely free from processing residue or specks. The average surface roughness of this subregion is reduced to 1.32 nm and the root mean square roughness is reduced to 1.60 nm .

irreversible and the film usually does not recover over these cavities. The collapse of the gold film, and its subsequent stiction to the cavity walls could be occurring due to excess acetone use prior to the contact-transfer step during fabrication. It can be speculated that some of the acetone on the transfer pad that has not evaporated, gets trapped between the gold film and some of the cavities in the spacer layer, when the substrate is brought into contact with the film on the transfer pad. The trapped film of acetone wets the cavity bottom and the gold

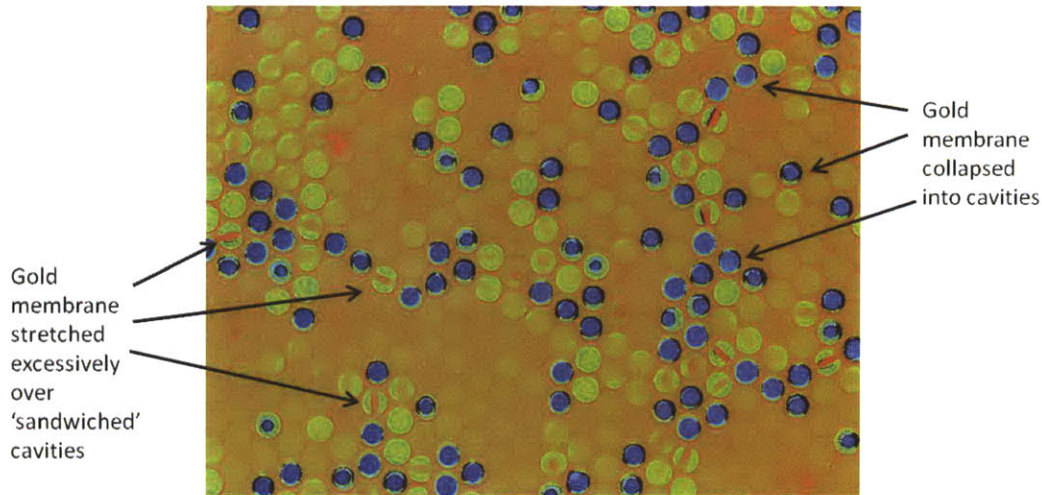


Figure 7.4: An optical interferometry image of a gold film contact-printed onto a cavity-patterned silicon dioxide spacer layer. Two main types of defects are observed. The gold film collapses over some cavities as it sticks to the cavity sidewalls and to the cavity bottom. This collapse of the gold film causes it to stretch irreversibly. The uncollapsed gold film over a cavity is excessively stretched when that cavity is surrounded by other cavities over which the gold film has collapsed. The excessive stretching causes the gold film to take on a peculiar shape, best described as a ‘ridge’ surrounded by a ‘basin’ on either side. The direction of the ridge is determined by the direction of excessive tension. Therefore, the ridge usually runs between two cavities with collapsed gold films, as shown above. If a cavity is surrounded by more than two cavities with collapsed membranes, then the direction of the ridge over the ‘sandwiched’ cavity is offset to account for the excessive tension from the surrounding collapsed-membrane cavities.

film. When pressure is applied prior to the lift-off step, the gold film on the relatively-compliant viscoelastic transfer pad comes into contact with the cavity bottom on the rigid substrate, and sticks to it. Figure 7.6 shows a cross-section profile of a gold membrane that has sunk in over one of the cavities in the spacer layer, obtained using optical interferometry. The profile of the gold membrane follows that of the cavity, and it is nearly vertical over the cavity circumference, as shown in Figure 7.5 as well. Additionally, the vertical distance from the gold membrane on top of a silicon dioxide support (in between adjacent cavities) to the gold membrane at the bottom of a cavity is about 950 nm, as indicated in

cross-section profile in Figure 7.6. This implies that the gold membrane sinks all the way to the bottom of the cavity. Since the gold membrane is only 125 ± 15 nm thick, and since it has to span the entire surface area of a ~ 27 - μm -diameter circular cavity, the membrane stretches—irreversibly—as it sinks over a cavity and covers its entire exposed surface. The surface area of a taut gold membrane suspended over a 27 - μm -diameter circular cavity is about 13% smaller than the total surface area of the same cavity that needs to be covered when a gold membrane sinks into it. In order to cover this excess area as it sinks over a cavity, the gold membrane stretches and, as a result, it pulls on the membrane region suspended over the adjacent cavities.

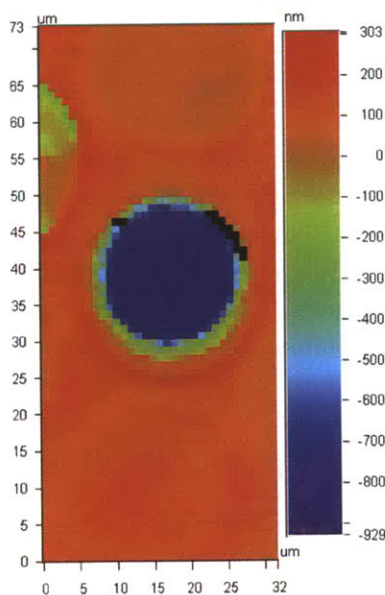


Figure 7.5: An optical interferometry image of a gold film that has collapsed over one of the cavities during the fabrication process. The thin green ring near the perimeter of the cavity indicates that the sunk-in gold film is nearly vertical at the cavity perimeter, as corroborated by the cross-section profile in Figure 7.6.

It is noticed that the region of the gold film that has sunk into a cavity cannot be “popped” back up using electrostatic force. A gold-wire probe is brought into

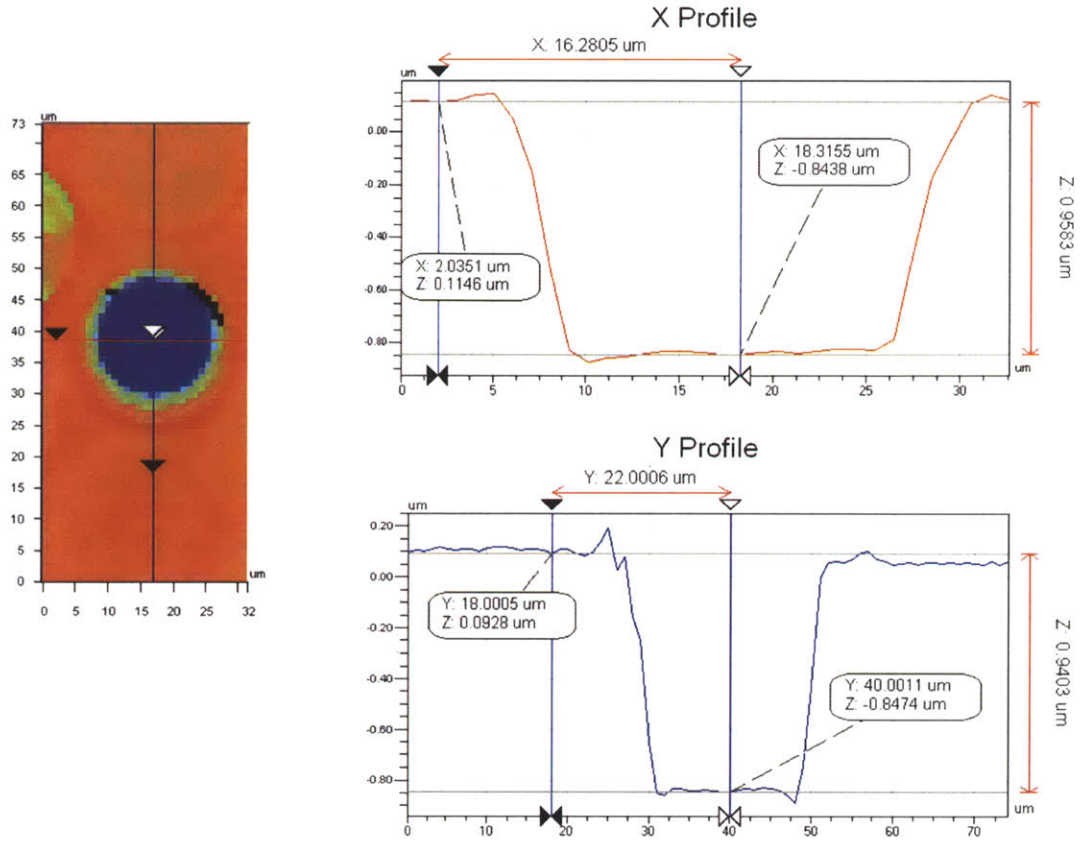


Figure 7.6: Cross-section profiles of a gold membrane that has collapsed over a cavity during the fabrication process. The vertical distance from the gold membrane on top of a silicon dioxide support (in between adjacent cavities) to the gold membrane at the bottom of a cavity is about 950 nm, as indicated above. This implies that the gold membrane sinks all the way to the bottom of the cavity.

contact with the gold film, and it is electrically grounded. Another gold-wire probe is then brought directly above the collapsed film region, but this probe is not in electrical contact with the film. A voltage is applied to the latter probe that hovers above the collapsed film region. The voltage is increased to 100 V. However, the electrostatic force between the gold-wire probe and the gold film is not enough to release the collapsed film. It can be speculated that the collapse of the gold film irreversibly stretches it beyond its elastic limit, making it difficult

for the film to recover into a suspended state above the cavity.

7.2.2 Excessive Stretching of Gold Membranes over Cavities

The aforementioned collapse of the gold film over cavities leads to a second type of defect observed in the transferred films. If a cavity is surrounded by other cavities over which the gold film has collapsed, then the gold film above this ‘sandwiched’ cavity stretches and deforms into the shape shown in Figure 7.7. The deformed shape consists of a central ‘ridge’ that spans the diameter of the cavity, and the ridge is in turn surrounded by a depressed ‘valley’ or ‘basin’ on either side. For the cavity shown in Figure 7.7, the highest point on the ridge rises about 200 nm above the planar surface of the gold film and the deepest point in the basins is about 300 nm below the planar surface of the gold film resting on the silicon dioxide supports, as shown in Figure 7.8. The maximum heights and depths of the ridges and the basins differ from one sandwiched cavity to the next. Furthermore, the direction of the ridge depends on the direction of the surrounding cavities with collapsed gold film regions, as shown in Figure 7.4. The gold film over a ‘sandwiched’ cavity deforms into the ridge and basins shape because of the cylindrically-asymmetrical tension exerted on either side of the gold film (over the sandwiched cavity) due to the strain resulting from the collapse of the film in the adjacent cavities. The deflection of these taut and deformed regions of the gold membrane over the ‘sandwiched’ cavities has yet to be characterized under applied bias.

Both of the aforementioned defects decrease the total number of cavities over which the gold membrane can deflect repeatedly. This leads to a compromised

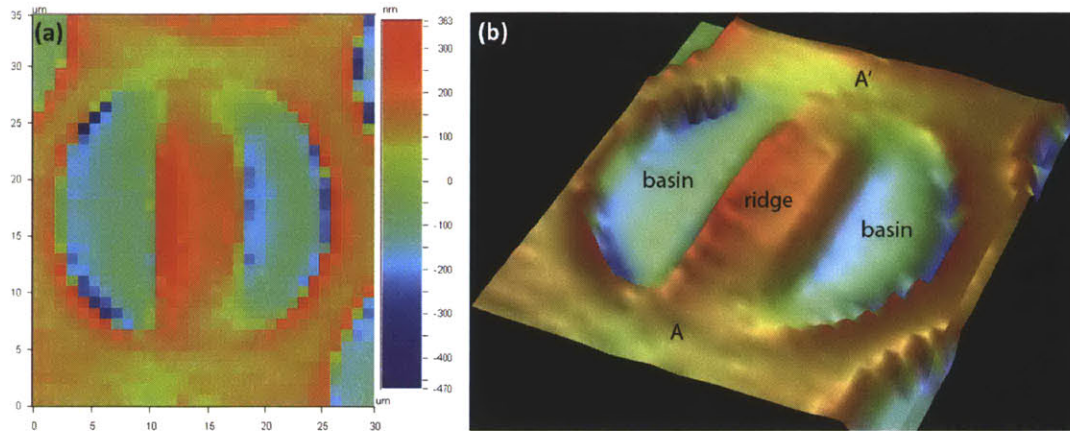


Figure 7.7: Optical interferometry images of an over-stretched gold film over a ‘sandwiched’ cavity, as shown in Figure 7.4. The cavity shown is surrounded by two cavities (not shown) over which the gold film has collapsed during the fabrication process. (a) A 2-D image of the sandwiched cavity. (b) A 3-D image of the sandwiched cavity obtained using interferometry data to highlight the elevated regions (the ridge) and the depressed regions (the basins) of the over-stretched gold film. The ridge spans the diameter of the cavity, and the two surrounding cavities over which the gold film has collapsed, are at either end of the ridge, as indicated by the points A and A’ on the figure.

overall device performance. For example, if the device is to be used for sound-producing applications in earphones and hearing aids, then the larger the number of aforementioned defects, the smaller the value of the sound pressure level produced. Additionally, a collapsed region of a gold membrane decreases the amount that the gold membrane can deflect over the adjacent cavities, at a given applied voltage, as shown in Figure 7.9. This further decreases the sound pressure level output. The membrane examined in Figure 7.4 is actually able to produce audible sound pressure levels, as discussed in Chapter 8. This means that the device will still function in the presence of the aforementioned defects, but not at the optimal performance level. Furthermore, the performance of the device will decrease as the number of these defects increases. This is in contrast to conventional capacitive MEMS devices where stiction usually results in complete device failure.

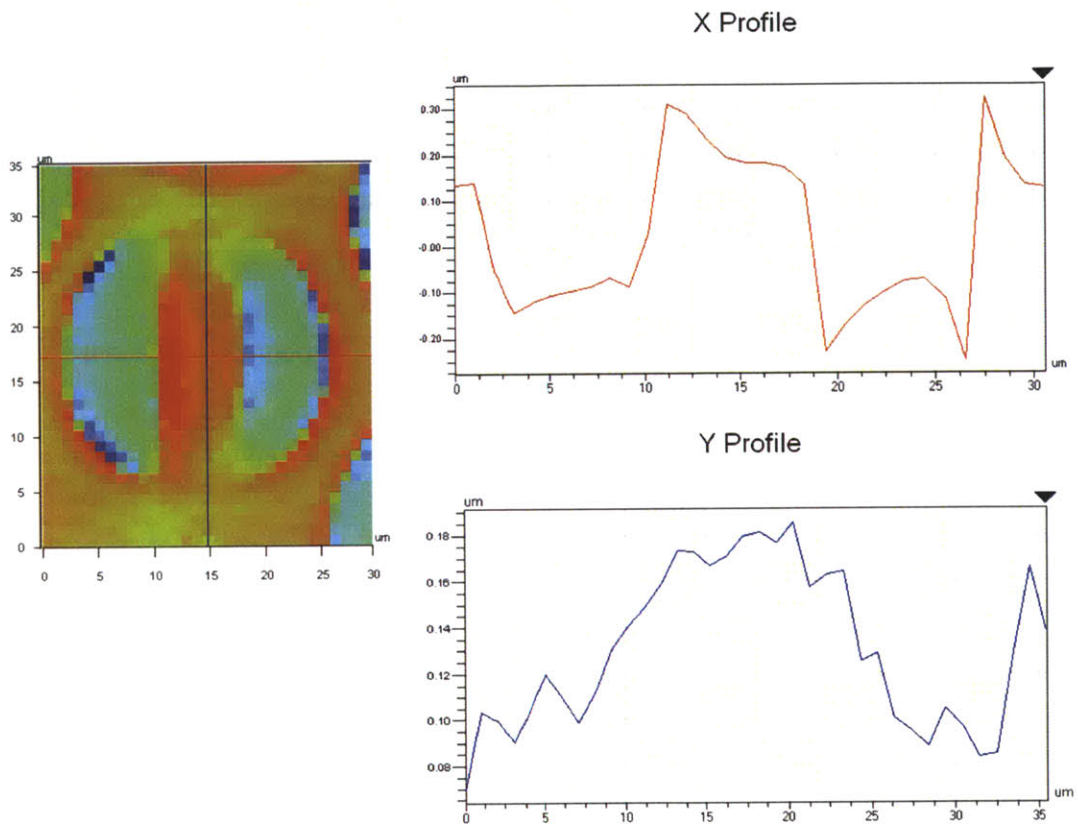


Figure 7.8: Cross-section profiles of the over-stretched gold membrane across a sandwiched cavity, as discussed in Figure 7.7. The profile in red is across the basins and the ridge of the gold membrane, showing that the ridge rises about 200 nm above the planar surface of the gold film and that the deepest point in the basins is about 300 nm below the planar surface of the gold film resting on the silicon dioxide supports. The profile in blue is across the length of the ridge.

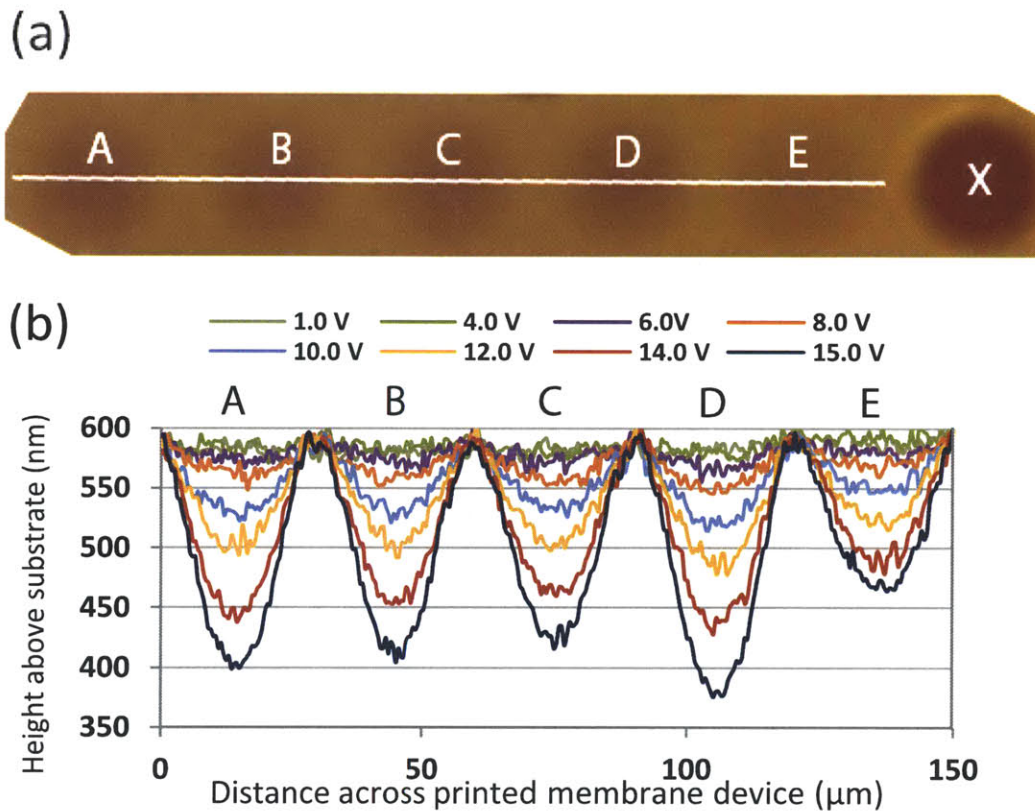


Figure 7.9: (a) Optical interferometry image of a gold membrane deflected over 400 nm deep cavities under 15 V applied bias. The white line indicates the cavities for which the deflection is plotted in (b) over various applied voltages. This line of cavities (A-E) is next to a cavity over which the gold membrane has collapsed due to fabrication, as indicated by 'X'. (b) Gold membrane deflection over multiple cavities as the voltage applied is increased from 1 V to 15 V. The deflection of the gold membrane over a cavity (E) next to a collapsed-membrane cavity (X) is significantly smaller than that of the membrane over cavities (A-D) further away from the collapsed-membrane cavity.

Chapter 8

A Prelude to Contact-Printed Acoustics

As shown in Chapter 6, Section 1.2, it is essential to fabricate MEMS devices by transferring gold films of areas larger than 1mm^2 , in order to produce the sound pressure levels (SPL) required for microspeaker applications in earphones and hearing aids (>90 dB SPL). The acetone-assisted contact-transfer method discussed in Chapter 5, Section 2, has low yield, and it necessitates the application of a relatively large amount of pressure, prior to the substrate lift-off step. Hence, the contact-transfer method specified in Chapter 5 is not suitable for the transfer of larger-area gold membranes using the parameters specified in that chapter. Therefore, some of the contact-transfer fabrication parameters are modified to effect the successful, repeatable transfer of large area gold membranes, with significantly higher yields.

1. PDMS transfer pad curing time

The curing time of the PDMS transfer pad, before it is peeled from the SU-8

master, is increased from 6 hours to about 37 ± 4 hours at $60\text{ }^\circ\text{C}$. Increasing the curing time increases the stiffness of the PDMS mesas [13][14], and this enables the delamination and transfer of films deposited on the mesas, with greater ease, and with the application of a relatively smaller amount of pressure, prior to lift off.

2. Silane concentration for substrate surface silanization

The surface of the silicon dioxide spacer layer is chemically treated with silanes to enhance the adhesion of gold films to the SiO_2 surface, as discussed in Chapter 5, Section 2.2. The concentration of 3-mercaptopropyltrimethoxysilane (MPTMS, Sigma-Aldrich) is increased from 0.001:1 by volume (in ethanol) to 1:5 by volume (in 2-propanol). Increasing the silane concentration increases the silane coverage of the silicon dioxide surface [15][16][17], hence, increasing the surface density of thiol groups on the silicon dioxide surface. This enhances the adhesion between the gold films on the transfer pad, and the silicon dioxide spacer layer, prior to lift-off.

3. Silanization time and temperature

The silanization time of the silicon-based substrates in MPTMS is increased from 24 hours to ~ 33 hours. The silanization temperature is increased from $80\text{ }^\circ\text{C}$ to $97\pm 2\text{ }^\circ\text{C}$. The silanization temperature and time are increased to effect a greater coverage of the silicon dioxide surface by the silane.

4. Silicon substrate cleaning prior to silanization

The silicon substrates with cavity-patterned silicon dioxide spacer layers are cleaned using the standard substrate cleaning procedure outlined in Chapter 3, Section 3. After cleaning, the substrates are treated with oxygen plasma for 5

minutes, to generate dangling bonds and hydroxyl groups on the surface of the silicon dioxide layer [18]. These hydroxyl groups bond with the methoxy groups on the MPTMS molecules during the silanization procedure via a condensation reaction.

The hydrophobicity of the silicon-based substrates increases after the MPTMS silanization, as confirmed by contact-angle measurements with water droplets.

The acetone-assisted contact-transfer process with the aforementioned modified parameters results in the successful repeatable transfer of large area, 125 ± 15 nm thick gold films onto cavity-patterned silicon dioxide spacer layers, and onto bare silicon substrates. In comparison to the parameters discussed in Chapter 5, the modified parameters enable the transfer of gold films onto silicon dioxide substrates with greater ease, and with the application of significantly less pressure (a light tap of tweezers on the substrate resting atop the transfer pad) prior to the lift-off step.

Membranes $\sim 12.5 \text{ mm}^2$ and $\sim 3.2 \text{ mm}^2$ in area are repeatedly transferred onto cavity-patterned silicon dioxide spacer layers using contact-transfer with the aforementioned fabrication parameter modifications, as shown in Figures 8.1 and 8.2. These membranes are up to 15 times larger than the ones transferred via the original acetone-assisted method discussed in Chapter X. The $\sim 12.5 \text{ mm}^2$ area films cover approximately 16000, $\sim 27\text{-}\mu\text{m}$ -diameter circular cavities, and the $\sim 3.2 \text{ mm}^2$ area films cover approximately 4000, $\sim 27\text{-}\mu\text{m}$ -diameter circular cavities. The qualitative yield (the area of gold picked-up and transferred per substrate) also increases significantly due to the aforementioned fabrication parameter modifications. Figure 8.2 shows two approximately $0.5'' \times 0.5''$ silicon substrates that are extensively covered in gold films transferred by the modified acetone-assisted contact-transfer process.

The effectiveness of the modified acetone-assisted contact-transfer process for transferring films smaller than 3.2 mm^2 in area has yet to be demonstrated.

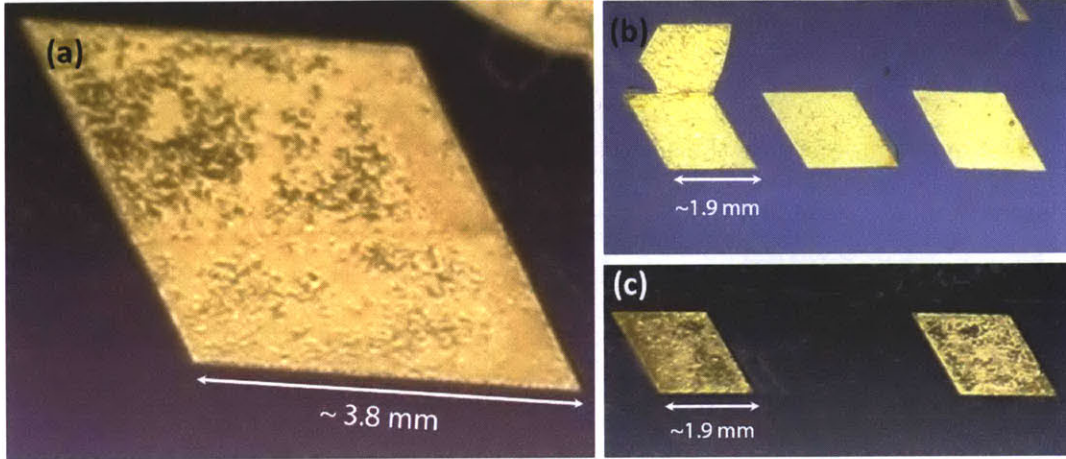


Figure 8.1: Photographs of large area gold membrane devices fabricated on cavity-patterned silicon dioxide substrates via acetone-assisted contact-transfer printing with increased transfer pad curing time and spacer layer silanization time, increased silane concentration, and increased silanization temperature. (a) A large area gold membrane covering about 16000, $27\text{-}\mu\text{m}$ -diameter cavities, in a single-sensor geometry. (b) and (c) Arrays of large area gold membranes, each covering about 4000, $27\text{-}\mu\text{m}$ -diameter cavities.

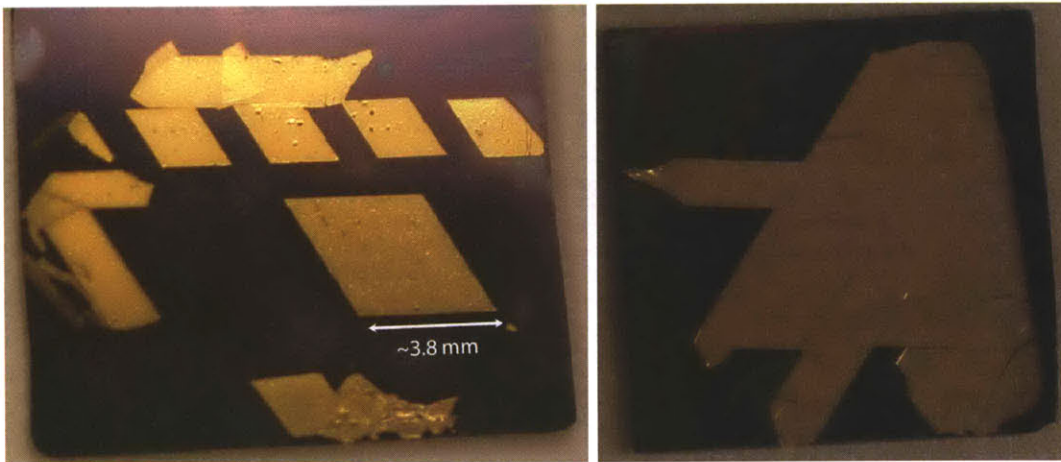


Figure 8.2: Photographs of two approximately $0.5'' \times 0.5''$ silicon substrates that are extensively covered in gold films transferred via the modified acetone-assisted contact-transfer process. The yield (the area of gold picked-up and transferred per substrate) increases significantly due to the modification of transfer pad fabrication and spacer pad fabrication parameters.

8.1 Sound Production

The aforementioned $\sim 12.5 \text{ mm}^2$ area gold film capacitive MEMS devices are electrically actuated to demonstrate sound production within the human auditory range. The silicon dioxide spacer layer in these devices is $\sim 1 \text{ }\mu\text{m}$ thick. The back of the substrate (silicon) is electrically grounded. A gold wire probe is brought into contact with the gold film atop the cavity-patterned silicon dioxide spacer layer, as shown in Figure 8.3. The output of a waveform generator (Tabor Electronics, Model WW2074) is fed to a high voltage amplifier (TEGAM Inc., Model 2350). The signal from the high voltage amplifier is then fed to the gold wire probe in contact with the gold film. A sinusoidally-varying voltage is applied to the device. The frequency and the peak-to-peak amplitude of this signal are varied.

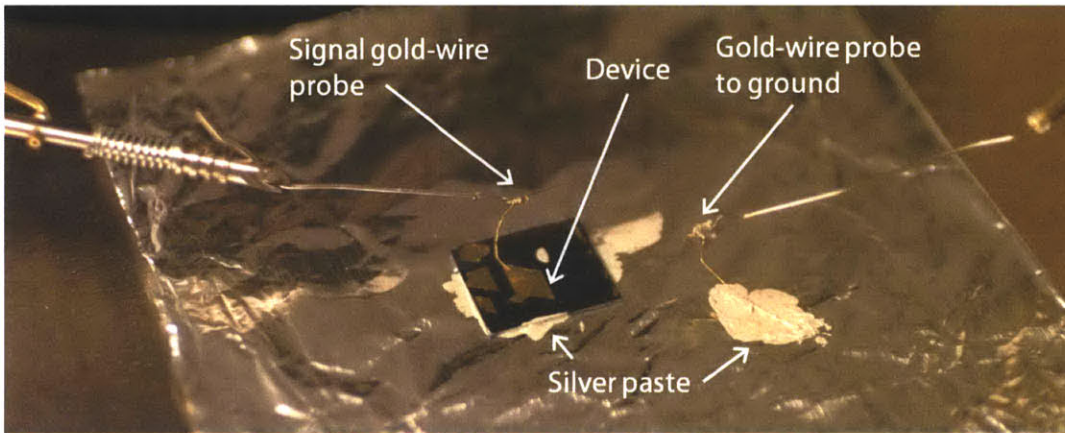


Figure 8.3: The electrical setup for preliminary sound production tests. The signal is being applied to the contact-printed device from the waveform generator via a high voltage amplifier. Electrical contact to the device is made using soft gold wire probes. Silver paste is used to improve electrical contact between the device substrate and the grounded aluminum foil.

Sound emitted by these capacitive MEMS devices is heard predominantly for 4 kHz to 13 kHz input frequencies. The loudest sound is produced at $\sim 12 \text{ kHz}$ input frequency. The peak-to-peak amplitude of the input signal is between 65 V

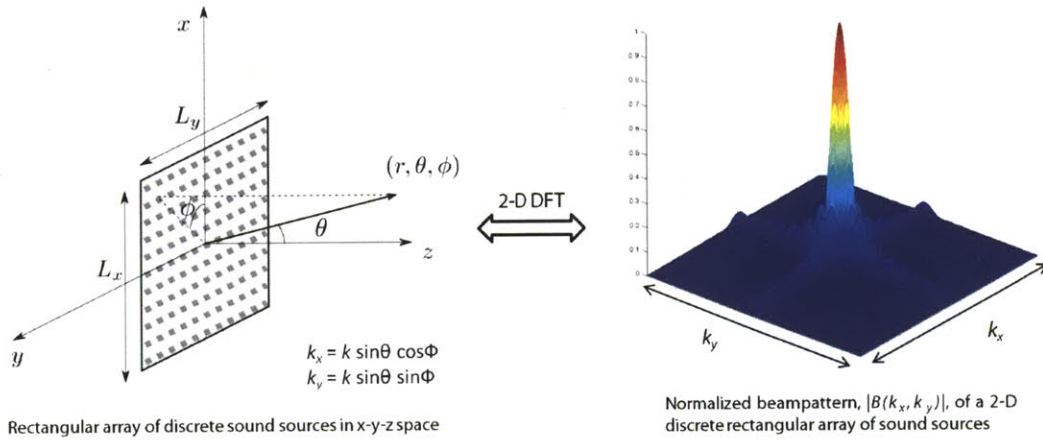


Figure 8.4: The far-field beam pattern for an unphased, two-dimensional, rectangular array of sound producing elements obtained by computing the 2-D discrete Fourier transform (DFT) of the rectangular array. The narrow main lobe in the beam pattern suggests that the loudest sound is heard on-axis, that is, directly above the gold film of the contact-printed device.

and 85 V. The sounds produced can be heard easily by a normal, human adult at a distance of ~ 7 cm from the device. Since the area of the sound producing element, that is, the gold film, is very small, the sound produced is very directional. The far-field beam pattern for an unphased, two-dimensional, rectangular array of sound producing elements, as shown in Figure 8.4, suggests that the loudest sound is heard on-axis ($\theta = 0$), directly above the gold film of the device.

Further characterization of sound production by these devices in an anechoic chamber is planned. However, from the aforementioned preliminary sound production data, it is evident that these contact-printed devices are suitable for microspeaker applications in earphones and hearing aids. Since the gold film in these devices was 125 ± 15 nm thick, the loudest sounds were heard primarily in the treble range. The frequency response of these devices can be improved to enable sound production in the lower human auditory range (bass, < 2 kHz) as well, by increasing the transferred film thickness.

A flat-frequency-response sound-producing device can potentially be achieved by transferring a graded film with varying thickness. If the film thickness varies continuously across the film length, multiple cavities can be bridged by a single film of varying thickness, as shown in Figure 8.5. Therefore in a single device, each cavity or a group of cavities (of constant or varying diameters) ends up being covered by a certain thickness (or a certain range of thicknesses) of the same conducting membrane. A graded film has the potential to improve device functionality in multiple ways:

- It could enable reversible transduction using the same printed device. A single printed device could potentially be used as a sensor (microphone for sound detection) or as an actuator (microspeaker for sound production), without significant performance decrease in either mode.
- It could enable the printing of microphones and microspeakers as two separate devices on a single substrate, in a single printing step. The substrate could be rigid (such as silicon or silicon dioxide) or flexible (polymeric or viscoelastic substrates such as PDMS). Additionally, for hearing aid applications, microphones and microspeakers could potentially be printed, in a single step, on two rigid substrates connected by a flexible substrate, such that the sound picked up by the microphone in one direction can be relayed to the microspeaker facing the opposite direction (the ear canal).

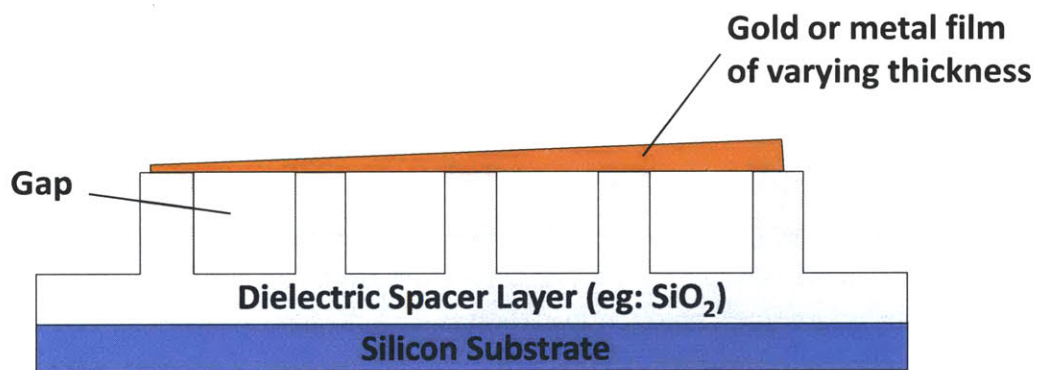


Figure 8.5: A cross-section schematic of a MEMS device with a contact-printed metal film. The thickness of the film varies across the length of the film such that multiple cavities or gaps are bridged by a single film of varying thickness. The bridged cavities can be commonly actuated or each cavity can be addressed individually. The drawing above is not to scale.

Chapter 9

Avenues for Further Research

In addition to device improvements outlined in the previous chapter for acoustic applications, there are several other areas where further progress can be made. A multitude of MEMS devices, in addition to pressure sensors and microspeakers, can be fabricated using contact-transfer printing on both rigid and viscoelastic substrates. Furthermore, the contact-transfer printing process can be combined with traditional integrated-circuit fabrication technologies to effect low-cost printed MEMS on silicon-based rigid substrates with CMOS circuitry. Film materials other than gold can also be investigated to extend the class of devices that are enabled by this printing technology. Some of these potential research avenues are outlined in greater detail below.

9.1 Device Geometry

Contact-transfer printing of gold membrane electrodes of areas larger than 12.5 mm² needs to be demonstrated to determine the scalability limits of this printing technology. Furthermore, large area membrane (> 4 cm² area) devices have the

potential for speaker applications in portable consumer electronics, such as tablet computers, and laptops. Devices with larger-area membranes are also capable of producing a larger signal-to-noise ratio.

Additionally, the capacitance change (at any given applied bias) of devices fabricated on PDMS substrates, as discussed in Chapter 4, can be increased by decreasing the thickness of the PDMS spacer layer. This can be achieved by decreasing the thickness of the spun-on SU-8 resist used to make the SU-8 master. The thickness of the residual PDMS layer in the cavities also needs to be decreased in order to increase the capacitance change of the devices at lower voltages. The thickness of the SU-8 resist can be decreased by diluting SU-8 with cyclopentanone, prior to spinning it onto the silicon wafer. Dilution with cyclopentanone makes the SU-8 resist less viscous, hence, enabling a thinner layer of the resist to be spun on top of the silicon wafer.

9.2 Transfer of Films of Different Metals and Graphene

It is highly desirable to demonstrate the repeatable transfer of thin films of metals other than gold. Various material properties (mechanical and optical) of different metals can potentially be exploited to fabricate a wide range of MEMS devices in addition to microspeakers, microphones, and pressure sensors. It is also valuable to explore the contact printing of graphene electrodes onto rigid and flexible substrates. Graphene electrodes printed atop patterned PDMS spacer layers on ITO substrates can potentially function as optically-transparent MEMS devices.

9.3 Stamping Apparatus

A stamping apparatus has to be developed to enable controlled application of force during the stamping process. Additionally, the stamping apparatus should enable micron-resolution placement of devices on substrates. The apparatus should rely on the process flow discussed in Chapters 3 and 5, to stamp devices on a substrate via controlled-force delamination. Optimally, the stamping apparatus should be capable of multi-layered alignment to a specific origin to enable the stamping of devices on substrates with specifically patterned electrodes that allow the addressing of specific sensors in an array.

9.4 Fabrication on Substrates with Patterned ITO-Electrodes

An addressable array of sensors (or actuators) is essential for enabling the phasing of these sensors. Therefore, it is necessary to be able to pattern electrodes on a substrate such that the data from each individual sensor in an array can be read, as shown in Figure 9.1.

One of the most difficult steps in characterizing the contact-printed devices is making good electrical contact with the top gold electrode. Currently, gold wire probes are used to make electrical contact with the gold films. However, placement of these gold probes, and, hence good contact with the gold membrane, is very sensitive to external disturbances, such as mechanical vibrations. For devices fabricated on PDMS spacer layers, a potential solution is to pattern the ITO layer on the glass substrate, prior to stamp fabrication. Patterning the ITO layer enables both of the electrical contacts to be made onto the ITO layer itself. These

contacts are more stable, and less vulnerable to external physical disturbances, and to the deflection of the gold membrane. Similarly, for devices fabricated on silicon dioxide spacer layers, the underlying silicon substrate could be replaced with a glass substrate with patterned metal electrodes for addressing individual cavities or groups of cavities.

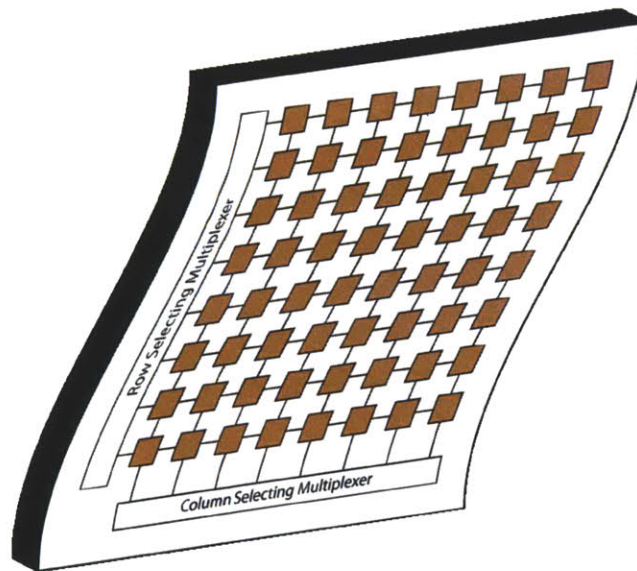


Figure 9.1: An illustration of a large-area array of individually-addressable sensors (or actuators) fabricated on a flexible substrate. Each element in the array can be addressed via the row-selecting and column-selecting multiplexers.

9.5 Phased Arrays of Sound Sources and Beam Steering

Our contact-transfer printing method enables the fabrication of thousands of potentially individually-addressable MEMS devices, over large areas. Therefore, the conventional cost, fabrication, and assembly barriers to achieving large-area phased arrays of sensors and actuators are now significantly mitigated. An imme-

diate demonstration would involve addressing individual cavities of the contact-printed sound source discussed in Chapter 8, such that the beam of sound produced by the entire device could be steered to a multitude of directions via phasing of the individual cavities.

9.6 Demonstration as Microphones

In addition to demonstrating deflection of the gold membrane under electrostatic loading, it is essential to demonstrate the deflection of the gold membranes under mechanical or pneumatic loading. These devices can potentially be used as microphones. A simple demonstration of this capability can be accomplished by attaching a current sensor to the contact-printed device to measure the current that flows into and out of the device as the membrane deflects under acoustic pressure, as shown in Figure 9.2, and as discussed in greater detail in Reference [19].

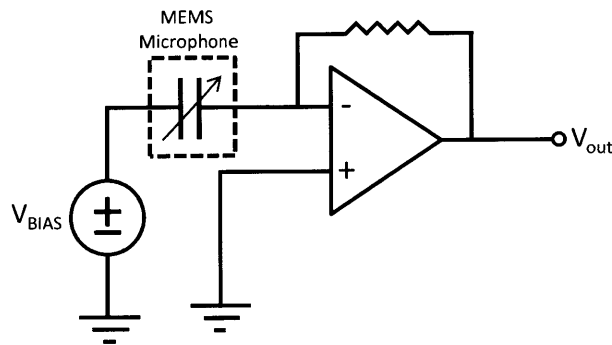


Figure 9.2: A simple current-sensing circuit implemented using an op-amp differentiator to detect capacitance changes of the MEMS device in response to an incident sound pressure wave.

9.7 Manipulation of Light Incident on a Surface

The reflectivity of a substrate can be modified by covering it with the aforementioned contact-printed membranes. The gold membranes of devices discussed in Chapter 6, exhibit both specular and diffused reflection. When the gold membranes are unbiased, and undeflected, the surface of the device is relatively smooth in regions where the membrane has not collapsed into the cavities. Any light shining on the device is reflected directionally, and the surface appears glossy due to specular reflection.

Interestingly, the reflectivity of the device surface can be changed by applying low voltage biases. When a voltage is applied between the gold membrane and the bottom silicon electrode, the electrostatic attraction between the membrane and the bottom electrode causes the electrode to deflect towards the bottom electrode. The greater the voltage applied, the greater the deflection. As the membrane deflects, the overall roughness of the device surface increases because of the deflected membranes over the cavities and the undeflected membranes over the support structures. This rough surface results in light being reflected in varying directions, and the surface appears matte due to diffused reflection. More specifically, when the surface of the membrane is uneven, the path difference—between the light reflected from the top of the support structure, and from the deflected membrane over the cavity—results in the reflected light interfering at the observer. When the path difference is large enough, the specularly reflected light intensity is low due to significant interference, hence, producing an effect similar to that of a rough surface scattering incident light in various directions. As shown in Figure 9.3, h is the minimum uniform deflection of the membrane necessary for the printed metal surface to meet the Rayleigh criterion for rough surface conditions

(reduced specular reflection). Table 1 shows the minimum membrane deflections necessary (for incident light of different wavelengths) to meet the Rayleigh criterion at various incidence angles. Membrane deflections greater than those specified in Table 1 will result in diffused reflection. The SiO₂ spacer layer devices discussed in Chapter 6 are able to achieve these deflections at 15 volts or less. These devices can potentially function as reconfigurable-reflectivity surfaces for angles of incidence up to 67° for 550-nm-wavelength light. The range of incidence angles can be further increased by simply increasing the thickness of the dielectric spacer layer.

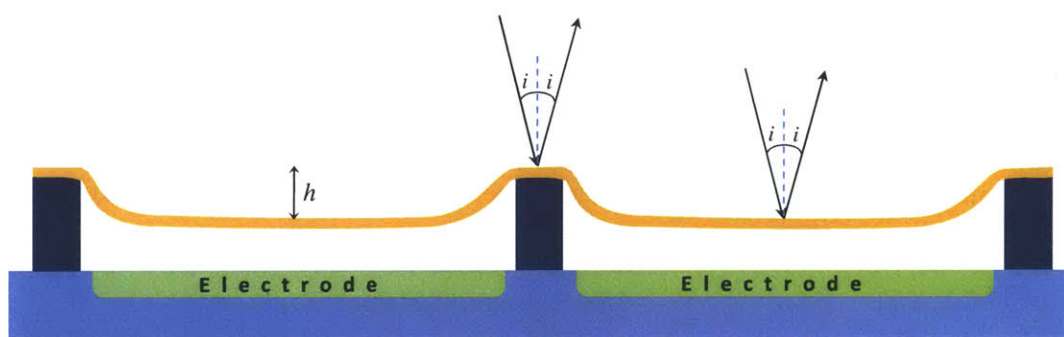


Figure 9.3: When the deflection, h , of the metal membrane is large enough, a significant portion of the reflected light intensity decreases due to interference, thus making the membrane covered surface appear rough. The devices discussed in Chapter 6 are able to achieve deflections that are large enough to produce the aforementioned effect for a wide spectrum of visible light, for angles of incidence up to 60°.

The roughness of the surface can be further increased by patterning the underlying spacer layer with cavities of different shapes and areas, resulting in sharper deflection profiles for membranes over non-circular cavities. The ability to print these thin metal membranes on both flexible and rigid substrates enables the potential demonstration of sensor skins with analog, electronically-controllable reflectivity. Additionally, by patterning the underlying electrodes, different regions of the metal membranes can be deflected by different amounts, hence enabling the

skin to exhibit spatially-varying reflectivity that can be reconfigured in real time using appropriate application specific integrated circuits.

Moreover, a substrate with a cavity-patterned spacer layer that is covered with these printed membranes can conceivably act as a directional mirror if the electrodes underneath the spacer layer are patterned as shown in Figure 9.4. The membrane can be made to deflect asymmetrically by switching on only one of the two electrodes underneath the membrane. The asymmetrical deflection of the membrane would cause the normal of the reflecting surface to rotate, hence changing the direction in which most of the light is reflected. The device shown in Figure 9.4 has three electronically-controlled digital states. This implies that it can specularly reflect light in three different directions. The number of digital directions that such a mirror has can potentially be increased by increasing the number of electrodes. The aforementioned MEMS device with electronically-controllable asymmetrical metal membrane deflection can be used to implement large area digital light processing systems for light projection applications.

Table 9.1: The minimum uniform deflection of metal membranes needed to make a reflecting surface appear rough through diffused reflection, for red, green, and blue light, at different angles of incidence of light.

Incidence Angle, i	Minimum deflection, h , needed for Rayleigh roughness		
	$\lambda = 680$ nm (R)	$\lambda = 550$ nm (G)	$\lambda = 420$ nm (B)
30°	98 nm	79 nm	61 nm
45°	120 nm	97 nm	74 nm
60°	170 nm	137 nm	105 nm
85°	975 nm	789 nm	602 nm

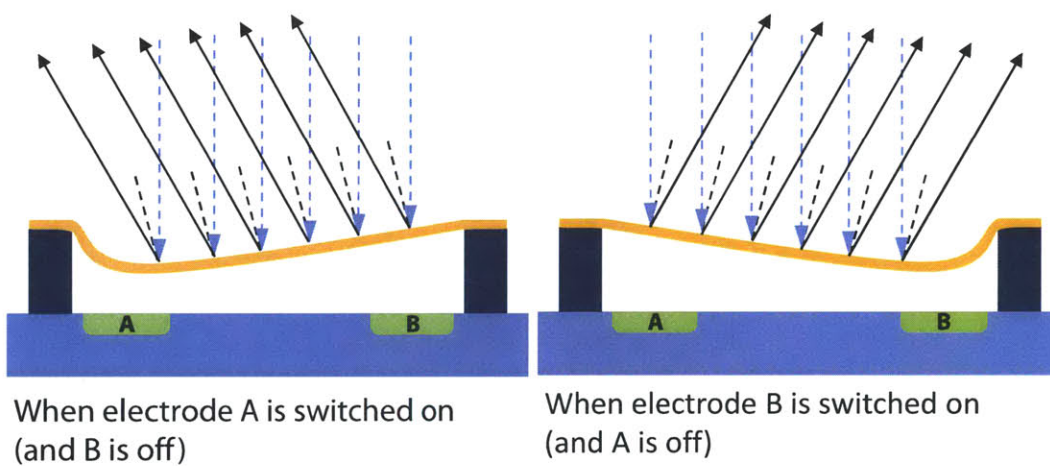


Figure 9.4: The blue arrows represent incident light and the black arrows represent reflected light. The metal membrane can be made to deflect asymmetrically by switching ON only one of the two electrodes, A or B. The asymmetrical deflection causes the normal of the reflecting surface to rotate, hence, changing the direction in which the incident light is reflected. The degree of asymmetrical deflection can be increased or decreased by increasing or decreasing the voltage applied to the ON electrode. When both electrodes are switched on or switched off, most of the incident light is reflected back in the incident direction.

Bibliography

- [1] C. Packard, A. Murarka, E.W. Lam, M.A. Schmidt, V. Bulovic, “Contact-Printed Microelectromechanical Systems”, *Advanced Materials*, vol. 22, pp. 1840-1844, 2010.
- [2] S. M. Spearing, “Materials issues in microelectromechanical systems (MEMS)”, *Acta Materialia*, vol. 48, pp. 179-196, 2000.
- [3] J. H. Daniel, R. A. Street, M. Teepe, S. E. Ready, J. Ho, Y. Wang, A. Rodkin, A. Alimonda, R. B. Apte, A. Goredema, D. C. Boils-Boissier, P.M. Kazmaier, “Large area MEMS: Materials issues and applications”, *Materials Research Society Symposium Proceedings*, vol. 685, pp. D.2.5.1-D.2.5.6, 2001.
- [4] M. A. Meitl, Z. T. Zhu, V. Kumar, K. J. Lee, X. Feng, Y. Y. Huang, I. Adesida, R. G. Nuzzo, J. A. Rogers, “Transfer printing by kinetic control of adhesion to an elastomeric stamp”, *Nature Materials*, vol. 5, pp. 33-38, 2006.
- [5] X. Feng, M. A. Meitl, A. M. Bowen, Y. Huang, R. G. Nuzzo, J. A. Rogers, “Competing Fracture in Kinetically Controlled Transfer Printing” *Langmuir*, vol. 23, pp. 12555-12560, 2007.
- [6] J. E. Mark, *Polymer Data Handbook*, Oxford University Press, New York, 1999.

- [7] S. Timoshenko, S. Woinowsky-Krieger, *Theory of Plates and Shells*, pp. 400-404, McGraw-Hill, 1959.
- [8] Y. Loo, R. L. Willett, K. W. Baldwin, J. A. Rogers, "Additive, nanoscale patterning of metal films with a stamp and a surface chemistry mediated transfer process: Applications in plastic electronics", *Applied Physics Letters*, vol. 81, pp. 562-564, 2002.
- [9] C. Kim, P. E. Burrows, S. R. Forrest, "Micropatterning of organic electronic devices by cold-welding", *Science*, vol. 288, pp. 831-833, 2000.
- [10] A. Murarka, S. Paydavosi, T.L. Andrew, A.I. Wang, J.H. Lang, V. Bulovic,, "Printed MEMS membranes on silicon", *Micro Electro Mechanical Systems (MEMS), 2012 IEEE 25th International Conference on*, pp. 309-312, Jan. 29 2012 - Feb. 2 2012.
- [11] A. Murarka, C. Packard, F. Yaul, J. Lang, V. Bulovic, "Micro-contact printed MEMS", *Micro Electro Mechanical Systems (MEMS), 2011 IEEE 24th International Conference on*, pp. 292-295, 23-27 Jan. 2011.
- [12] M. C. Cheng, W. S. Huang, and R. S. Huang, "A silicon microspeaker for hearing instruments", *Journal of Micromechanics and Microengineering*, vol. 14, pp. 859-866, 2004.
- [13] D. T. Eddington, W. C. Crone, D.J. Beebe, "Development of process protocols to fine tune polydimethylsiloxane material properties", *7th International Conference on Miniaturized Chemical and Biochemical Analysis Systems*, pp. 1089-1092, 2003.

- [14] O. du Roure , A. Saez, A. Buguin, R. H. Austin, P. Chavrier, P. Siberzan, and B. Ladoux, “Force mapping in epithelial cell migration”, Proceedings of the National Academy of Sciences, vol. 102, pp. 2390-2395, 2005.
- [15] A.R. Ladhe, P. Frailie, D. Hua, M. Darsillo, and D. Bhattacharyya, “Thiol-functionalized silica-mixed matrix membranes for silver capture from aqueous solutions: experimental results and modeling”, Journal of Membrane Science, vol. 326, issue 2, pp. 460-471, 2009.
- [16] M. Hu, S. Noda, T. Okubo, Y. Yamaguchi, and H. Komiyama, “Structure and morphology of self-assembled 3-mercaptopropyltrimethoxysilane layers on silicon oxide”, Applied Surface Science, vol. 181, issues 3–4, pp. 307-316, 2001.
- [17] A. J. Nijdam, M. M. Cheng, D. H. Geho, R. Fedele, P. Herrmann, K. Killian, V. Espina, E. F. Petricoin III, L. A. Liotta, and M. Ferrari, “Physicochemically modified silicon as a substrate for protein microarrays”, Biomaterials, vol. 28, issue 3, pp. 550-558, 2007.
- [18] S. Choi, W. Choi, Y. Lee, B. Ju, M. Sung, and B. Kim, “The analysis of oxygen plasma pretreatment for improving anodic bonding”, Journal of the Electrochemical Society, vol. 149, pp. G8-G11, 2002.
- [19] S. Peng, M. S. Qureshi, P. E. Hasler, N.A. Hall, F. L. Degertekin, “High SNR capacitive sensing transducer”, Circuits and Systems, ISCAS 2006 Proceedings, 2006 IEEE International Symposium on, pp. 1175-1178, 21-24 May 2006.